International Journal of Coal Geology 261 (2022) 104081

Contents lists available at ScienceDirect

International Journal of Coal Geology

journal homepage: www.elsevier.com/locate/coal

Characterizing mechanical heterogeneity of coal at nano-to-micro scale using combined nanoindentation and FESEM-EDS

Ang Liu [a], Shimin Liu [a,*], Yiwei Liu [b], Bangzhi Liu [c], Ting Liu [d]

[a] Department of Energy and Mineral Engineering, G3 Center and Energy Institute, The Pennsylvania State University, University Park, PA 16802, USA
[b] School of Civil Engineering, Wuhan University, Wuhan, Hubei 430072, China
[c] Materials Research Institute, The Pennsylvania State University, University Park, PA 16802, USA
[d] School of Safety Engineering, China University of Mining & Technology, Xuzhou, Jiangsu 221116, China

ARTICLE INFO

Keywords:
Nanoindentation
Heterogeneity
FESEM-EDS
Proppant embedment

ABSTRACT

The variations of mechanical properties of coals in nano-to-micro scale play vital roles in defining the coal deformative and failure behaviors with a wide range of engineering applications, including coal stimulation for gas recovery and/or CO_2 sequestration in coal seams. Based on the assumption that the heterogeneity in the mechanical properties of coals is combinedly determined by the mineralogical/carbon compositions and microstructures, three coals were experimentally measured through combing nanoindentation test, X-ray diffraction (XRD) analysis and field emission scanning electron microscopy - energy dispersive spectroscopy (FESEM-EDS) imaging. Two sub-bituminous coals from Illinois basin and one bituminous coal from Pittsburgh No.8 seam from Pennsylvania were collected and prepared. The moduli, hardness, and energy dissipations were all analyzed for three coals. The mean Young's moduli and hardness of two sub-bituminous and bituminous coals are ~4.13 GPa, ~4.79 GPa, and ~ 5.56 GPa respectively and the mean hardness of which are ~0.38 GPa, ~0.49 GPa and ~ 0.58 GPa respectively. The results confirmed that the nanoscale mechanical properties are compositional and microstructural dependent. It was also observed that the heterogeneity of sub-bituminous coals is more apparent than the bituminous coal. Also, the bituminous coal is more harder and brittle than sub-bituminous coal, which can better withhold the mechanical response, but the deformations are relatively permanent due to brittle failure. The energy dissipation data showed that the irreversible work decreases with the increase in hardness, which confirmed that the plastic deformation is much more easily to be inducted. The mechanism-based phenomenon pop-in event on the load-displacement curve was also analyzed by linking with the characteristics of the morphology and composition beneath a pointed indenter or cracks formation due to the localized indent.

1. Introduction

Coal is inherently heterogeneous with complex nano- and micro-scale structures and mineralogical compositions because of the complicated coal metallogeny (Li et al., 2022c). Extensive studies have been conducted on the mechanical properties of coal, such as strength (*i.e.* uniaxial compressive strength, shear strength, tensile strength, et al.), hardness, elastic properties (Young's modulus, bulk/grain modulus, Poisson's ratio, *etc.*), compressibility, and Biot's coefficient, and the deformative responses through meso- or macroscopic laboratories (Bandyopadhyay et al., 2020; Dou et al., 2021; Kim et al., 2021; Zuo et al., 2019). However, the meso- or macro-scale laboratory measurements did not directly provide the mechanical parameters and predict the failure behavior of coal with different compositions and anisotropies in nano- and micro- length scale.

As an example, coal formation permeability is directly influenced by the sandwiching stress on proppant packs during hydraulic fracturing stimulation. Due to proppant crushing and embedment induced by the sandwiching stress on proppant packs, the maximized permeability at the beginning stage after hydraulic fracturing cannot be properly maintained and may exhibit reduction trend (Masłowski and Labus, 2021). Proppant damages include proppant crushing, proppant embedment due to the limited surface contact and the intensive stress concentration, which may create formation fines in micro- or nano- scale and results in excessive loss of fracture conductivities (Masłowski and Labus, 2021). Even though it is conceptually understandable that the

* Corresponding author.
E-mail address: szl3@psu.edu (S. Liu).

https://doi.org/10.1016/j.coal.2022.104081
Received 9 March 2022; Received in revised form 3 August 2022; Accepted 8 August 2022
Available online 10 August 2022

proppant damage or proppant embedment can lead to fracture conductivity loss, the microscopic mechanics remains un-quantified due to the heterogeneity of coals. As another example, the localized coal damage or straining can be caused by the combined effects of matrix shrinkage and the evolutions of *in situ* stress (Liu et al., 2021; Liu et al., 2020), which occurs mainly due to the strength difference in mineralogical compositions and the complex distributions of microstructures under the equivalent stress condition (Liu and Harpalani, 2014; Lu and Connell, 2016, 2020). Understanding and quantifying the mechanical properties of coals in micro- or nano-scale originating from the variability in their mineral and structural compositions plays a vital role in designing safe and cost-efficient mining, optimizing hydraulic fracturing, maximizing the long-term production of coalbed methane (CBM) reservoirs, and enhancing CO_2 sequestration in coal seams (Manjunath and Jha, 2019).

Advanced characterization techniques have been adopted to investigate the distinct features of heterogeneous geomaterials. Nanoindentation, a non-destructive technology which can measure the mechanical properties of the materials in micro- and nano-scale (Fischer-Cripps, 2011). It has been introduced to the measure the mechanical properties including Young's modulus, hardness, fracture toughness, residual stress, elastic and plastic work, *etc.* of different rocks such as coal (Epshtein et al., 2015; Kossovich et al., 2019; Manjunath and Jha, 2019), shale (Li et al., 2022a, 2022b; Sharma et al., 2019; Shi et al., 2020a, 2020b), and other rocks such as sandstone, claystone, granite, et al., as summarized in Ma et al. (2020). Zhang et al. measured the mechanical properties of a sub-bituminous coal at microscale through nanoindentation test and compared that with the centimeter-scale acoustic measurements. The moduli measured from nanoindentation significantly varied from 1 GPa to 60 GPa, which are obviously correlated with the coal morphology based on the scanning electron microscopy (SEM) imaging and micro-CT analyses. But the acoustic measurements showed that the moduli of the centimeter-scale bulk coals range from 2.41GPa to 3.32GPa (Zhang et al., 2018). In case of multiphase and heterogeneous materials, other valuable insights into the heterogeneity of microstructural have been obtained by using coupled atomic force microscopy (AFM) and instrumented indentation on geomaterials (Prasad et al., 2002). In addition, a combination of grid nanoindentation and SEM with Energy and Wavelength Dispersive X-ray Spectrometry (EDS/WDS) at the same spatial locations to identify both the nano-mechanical morphology and local mineralogy of these nanocomposites were also characterized on shales (Veytskin et al., 2017).

From the load–displacement curves acquired *via* the nanoindentation tests, phenomena such as pop-in or chipping, elbowing, and pop-out were commonly observed (Kasyap, 2021). A pop-in (event) is a sudden (load or displacement) burst during the loading of an indenter on the sample. Typically, the pop-in event at the loading stage is often explained by the following mechanisms as a function of the indented specimen (*i.e.* ceramic, metal, semiconductor, coated or multilayer specimen, *etc.*) and the experimental conditions (*i.e.* time, temperature, geometry of the indenter, and others). The mechanisms such as dislocations nucleation (sudden yielding of a material under load) (Pöhl, 2019; Wang et al., 2022), rupture of a hard brittle film on an elastic-plastic substrate (Pethica and Tabor, 1979; Mercier et al., 2017), strain transfer across grain boundaries in metals (Javaid et al., 2020; Wang and Ngan, 2004), crack(s) formation (Bull, 2011; Hervas et al., 2016; Malzbender and De With, 2001), phase transformation (Furnémont et al., 2002; Huang and Yan, 2015) and others (Oliver et al., 2007; Szlufarska et al., 2004). A recent work used the brittle failure theory and fracturing-induced pop-in events in the loading curve to estimate the fracture energy and the fracture surface area of coal (Manjunath and Jha, 2019). The developments of pop-ins were particularly highlighted for shales and one study reported that the pop-in events are directly related to the cracks and pores in the shale rock, and further observed that the pop-in events influence the hardness values more pronouncedly compared with the elastic modulus (Wang et al., 2019). Due to the limited experimental measurements, the in-depth understandings of nanoindentation tests on coals and the underlying nanoscale mechanical properties and responses of coals under loads remains unclear.

In this study, based on the assumption that the heterogeneity in the mechanical properties of coals is controlled by the mineralogical/carbon compositions and microstructures, three coals were measured using the experimental method through combing grid-based nanoindentation test, X-ray diffraction (XRD) analysis and field emission scanning electron microscopy - energy dispersive spectroscopy (FESEM-EDS) imaging. We used the nanoindentation data and FESEM-EDS analyses to characterize the nanoscale deformation responses of three coals in terms of its modulus, hardness, and energy dissipation. The mechanism-based phenomenon pop-in events in the load-displacement curves were analyzed to provide the basis for the micron-scale mechanical behaviors. Since coals enrich with organic matter and generally the nanoindentation mechanical properties of these organic matter are expected to exhibit homogeneous characteristics. However, the occurrence of minerals in different coal, even in less amount, will introduce significant differences in mechanical properties. In an arbitrary nanoindentation area in nano- to micro-scale, the mechanical heterogeneity is expected to be significantly influenced by the minerals. Therefore, the nanoindentation results on the clusters of indents related to minerals are mainly discussed. In addition, it needs to point out that the nano- to micro-scale nanoindentation results can provide sound and fundamental evidence in nano- to micro-scale, rather than giving persuasive conclusions for a bulk coal before answering the multiscale question.

2. Materials and methods

2.1. Sample collection and preparation

To validate our hypotheses, coals with different mineralogical compositions and microstructures are expected to be measured. Three fresh coal samples, two sub-bituminous coals from Illinois basin (Springfield seam (I5) and the Herrin seam (I6)) and one bituminous coal from Pittsburgh No.8 seam (P8) from Pennsylvania, were collected from active mines.

For the microstructural analysis using the FESEM-EDS and nanoindentation test, the thin section preparation is crucial and the procedure was illustrated in Fig. 1. A thin chip with rough surface was cut from a bulk coal sample using cutter saw (Fig. 1 (a)). Then the thin section was placed into a cylindrical mold for casting using epoxy resin that consists of the epoxy resin and hardener by weight of 5:1 (Fig. 1 (b)). The epoxy resin was allowed to completely cure with the setting time of around 72 h before moving from its curing position (Fig. 1 (c)), which can prevent the sample from spalling or damaging during the surface preparation (Liu and Liu, 2022). The surface of the prepared thin section was further grinded and polished using the MultiPrep™ Polishing System to significantly reduce its roughness for the nanoindentation (Allied High- Tech Products, Inc.), as shown in Fig. 1(d). The abrasive sandpapers with grit sizes of 320, 600, 800, and 1200 were sequentially used to polish the testing surface of the sample. The water-free and alcohol-based lubricants and ethanol were used at this stage to smooth this process and avoid potential mineral hydrations. Then, the sample was further polished to reach a finer surface using 1 μm, 0.25 μm polycrystalline diamond suspensions followed by 0.05 μm alumina suspension. To avoid potential mineral hydrations at this stage, the suspensions were either ethylene- or glycol-based (Liu and Liu, 2022). Finally, the ethanol followed by the pressurized clean air was used to clean the prepared surface. All three prepared coal samples were firstly conducted nanoindentation tests followed by FESEM-EDS imaging and elemental analyses.

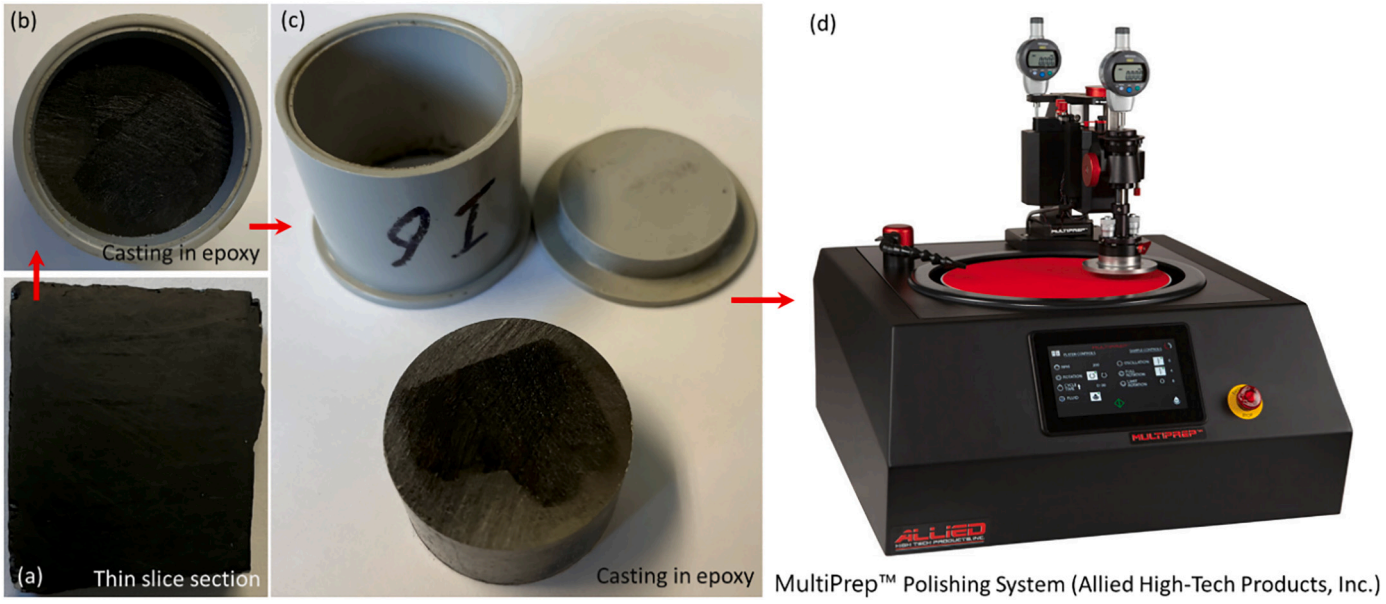

Fig. 1. Coal sample preparation for nanoindentation test and FESEM-EDS analysis.

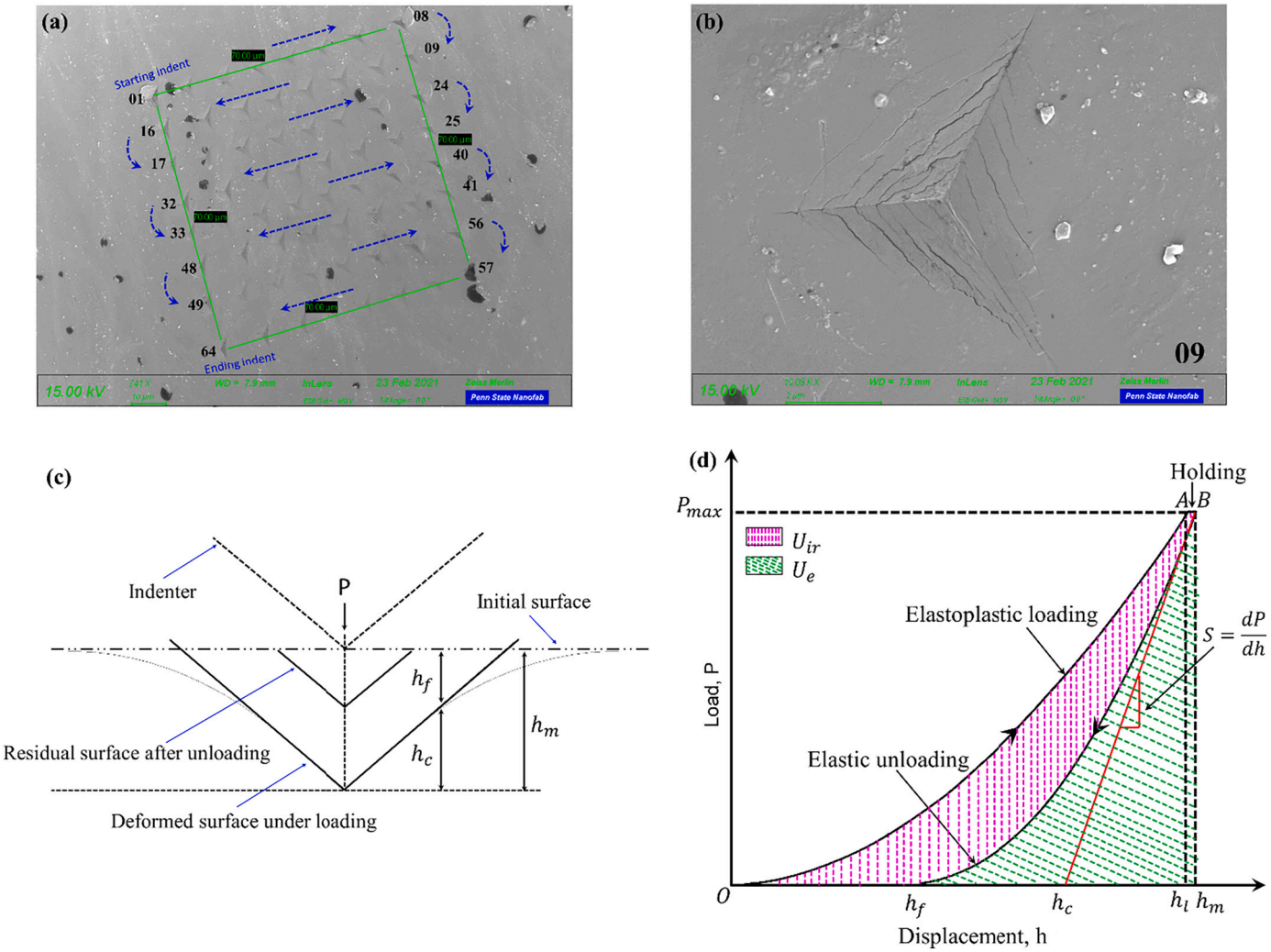

Fig. 2. Scheme of the loading-holding-unloading for nanoindentation test and the load-displacement curve.

2.2. Nanoindentation testing

The elastic and fracture properties of a material can be extracted from the indentation load-displacement data obtained during one cycle of loading, holding, and unloading. Although taking the holding stage at the maximum load is not mandatory to measure the elastic and fracture properties of a material by nanoindentation, the loading-holding-unloading scheme is often adopted to obtain stable data in this method (Jin et al., 2015; Zeng et al., 2017). In this study, the three-sided symmetric shape Berkovich indenter with the known Young's modulus (*i.e.* 1141 MPa) and the Poisson's ratio (*i.e.* 0.07) equipped with the Bruker Hysitron TI 980 (Bruker Corporation) was used for nano-indentation tests (Oliver and Pharr, 1992). The loading (0.5 s) - holding (0.2 s) -unloading (0.5 s) scheme of each indent with the maximum load of 10,000 nN was applied. We conducted 256 indents on four locations with each location has an 8×8 grid with 10 μm grid spacing for each of the three coal samples, as shown in Fig. 2 (a). The four locations were marked as M1, M2, M3 and M4. The 64 indents within the 8×8 grid were sequentially acquired *via* adjusting the position of indenter initially start from the top left corner, then to the top right corner by following the arrows. After completion of 8 indents in the row, the indenter was back to the next row from left to right. As shown in Fig. 2 (d), from the $(P-h)$ curve, five important quantities should be measured and recorded, including the maximum load, P_{max}, the displacement at the end of the loading stage h_l, the maximum displacement h_m, the final depth h_f (Fig. 2 (c)), and the elastic unloading stiffness, $S = dP/dh$, defined as the slope of the upper portion of the unloading curve during the initial stages of unloading. The deformation during the loading stage is supposed to be both elastic (reversible with unloading) and plastic (irreversible with unloading) as the permanent hardness impression forms (Liu and Liu, 2022). The reduced modulus (E_r) combines the modulus of the indenter and the specimen, which can be expressed as (Timoshenko and Goodier, 1951):

$$E_r = \frac{\sqrt{\pi}}{2\beta}\frac{S}{\sqrt{A_C}} \approx 0.17\frac{S}{h_c} \tag{1}$$

where, $A_c = 24.5h_c^2$ has been used as the contact area and $\beta = 1.034$ has been used as the geometric constant of a Berkovich indenter. The contact depth (h_c) can be calculated as $h_c = h_m - h_f$ based on Fig. 2 (c). Further, the relations among the reduced modulus, and the Young's moduli and the Poisson's ratios of the specimen and of the indenter can be expressed as (Sneddon, 1965):

$$\frac{1}{E_r} = \frac{1-\nu^2}{E} + \frac{1-\nu_i^2}{E_i} \tag{2}$$

where E, E_i, υ, ν_i are the Young's moduli and the Poisson's ratios of the specimen and of the indenter, respectively.

In addition, the expression proposed by Oliver and Pharr was used to represent the hardness (H) from the load-displacement curve (Oliver and Pharr, 1992),

$$H = \frac{P_{max}}{A_C} \tag{3}$$

2.3. Sample structural and compositional characterizations

2.3.1. Microstructural analysis

For a selected region, as shown in Fig. 2 (a), the indents were evenly distributed in an area of ~70 μm×70 μm grid plane. The variations of mechanical properties of coals in micro−/nano- scale can be attributed from the variability of mineral compositions and structural heterogeneity. The measured load-displacement curves were expected to show site-dependent (*i.e.* mineral- and micro structures- dependent) variations. To link the differences in the features of load-displacement curves for any given specific site, the FESEM-EDS was employed to probe the compositional and structural properties, as shown in Fig. 2 (a) and (b). The fabric of coal surface and its elemental compositions especially the targeted area has indent matrix were identified by Zeiss Merlin (Carl Zeiss AG). The basic parameters including vacuum pressure, acceleration voltage, aperture size, *etc* are very critical parameter settings. Since the surface roughness and conducting capacity of samples are different from sample to sample mainly due to the distributions of mineral/organic carbon compositions, the acceleration voltage for each case was always adjusted among 5 kV, 10 kV, 15 kV, 20 kV, and 25 kV, as can been seen in each FESEM image. To obtain an appropriate EDS resolution and pertinent size, the acceleration voltage is normally adjusted to obtain the dead time between 10% to 30%. In addition to acceleration voltage, the system vacuum pressure is always 2.75×10^{-06} Torr and the gun vacuum pressure is always 7.50×10^{-10} Torr. The standard aperture size 30 um is used in this study. The FESEM-EDS can identify the distributions and compositions of elemental variations but it cannot determine the crystalline phases (*i.e.* minerals) or amorphous phase (*i.e.* organic carbon). By combining with XRD results, the localized mineral/organic carbon compositions of indents can be identified, as illustrated in Appendix A.

2.3.2. Characterization of mineralogical compositions

To closely identify the minerals or organic carbon within tested coals, the coal specimen after the FESEM-EDS was initially cut to remove the epoxy and then was grounded using hand grinding to pass through a 325-mesh sieve. The mineral compositions of coal samples were analyzed by XRD using the Malvern Panalytical diffractometer (Malvern Panalytical Ltd.). For all three samples, the fresh fragments were pulverized to 325-mesh powders for XRD measurement. Coal powders were back-loaded into a reflection-transmission sample holder and diffraction data were collected from 5 to 70° 2θ using a a Malvern Panalytical Empyrean® instrument fitted with a copper long-fine-focus X-ray tube operated at 45 kV and 40 mA. The sample was spun at a speed of 1 rotation per second during the data collection. The incident beam path included iCore® optics fitted with a BBHD® optic with 0.03 rad Soller slits, a 14 mm mask, and a fixed 0.25° divergence slit. The diffracted beam path incorporated dCore® optics with a 0.25° fixed anti-scatter slit, a 14 mm mask, and 0.04 rad Soller slits. A PIXcel3D® detector was used in scanning line (1D) mode with an active length of 3.347° 2θ. Data were collected with a nominal step size of 0.026° 2θ. Phase ID and semi-quantitative analysis was carried out using Jade® software (version 8.5) from Materials Data Inc. (MDI) and the International Centre for Diffraction Data (ICDD) PDF4® database. Based on FESEM-EDS results, the distributions of these minerals can be identified. As an example, for identifying three different minerals such as pyrites (FeS_2), gypsum ($Ca(SO_4)(H_2O)_2$) and szomolnokite ($Fe(SO_4)(H_2O)$), the difference between pyrite and gypsum can be identified through the elemental mapping of Fe or Ca, the difference between pyrite and szomolnokite can be identified through the elemental mapping of O, while the difference between gypsum and szomolnokite can be identified through the elemental mapping of Fe (Liu and Liu, 2022).

2.4. Theory basis of nanoindentation test

2.4.1. Stress field beneath pointed indenter

The stress distribution in an elastic half-space subjected to a normal point load P is shown in Fig. 3. This is the so-called Boussinesq problem, and the solution of which in the axisymmetric system (r, ϕ, z) are given by (Lawn and Swain, 1975; Manjunath and Jha, 2019):

$$\sigma_{ij} = \left(P/\pi R^2\right)\left[f_{ij}(\phi,\nu)\right] \tag{4}$$

where, σ_{ij} is the Boussinesq stress; R is the radial distance; ϕ is the vertical angle from the load axis; ν is the Poisson's ratio. As illustrated in Fig. 3 (b), the radial stress σ_{rr} is tensile for a given ϕ, which indicates the potential for tensile fractures. The maximum principal stress is the

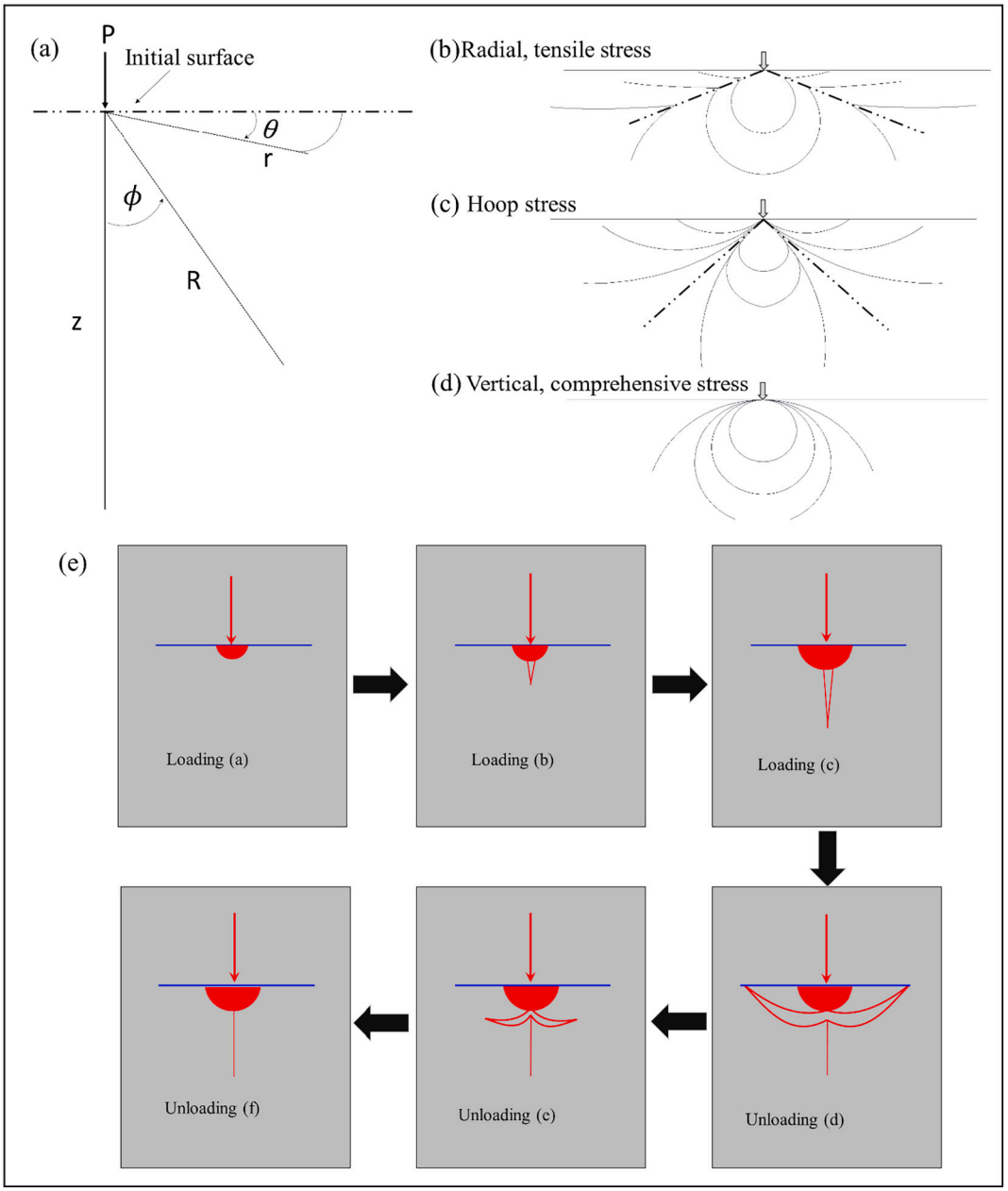

Fig. 3. Coordinate system for axially symmetric point loading *P* (a) and the contours of principal normal stresses in the Boussinesp stress field; (b) The maximum principal stress; (c) the hoop stress; (d) the minimum principal stress; (e) Schematic of vent crack formation under point indentation (Lawn and Swain, 1975).

tensile with a minimum value along the dotted lines and a maximum value on the surface, *i.e.* $\phi = \frac{\pi}{2}$. The hoop stress changes from being tensile below the indenter to being compressive near the surface based on the value of ϕ, the two regions are separated by the dotted lines (Fig. 3 (c)). The minimum principal stress is always compressive (Fig. 3 (d)) (Manjunath and Jha, 2019). A general pattern of behavior of indentation-induced microcracking has been established based on a wide range of experimental conditions considering the materials, the pointed indenters, and testing machines (Lawn and Swain, 1975). The essential features of the pattern can be described as (Fig. 3 (e)): (a) the irreversible deformation at the initial loading stage (Loading (a) in Fig. 3. (e)); (b) following by the critical zone forming stage, under some critical indenter load a tensile crack suddenly initiates below the contact point where the stress concentration is greatest (Loading (b) in Fig. 3. (e)); (c) during the stable crack growth stage, the stable extension of the crack will occur with the increasing load (Loading (c) in Fig. 3. (e)); (d) once initial unloading stage starts, the crack begins to close but not heal (Unloading (d) in Fig. 3. (e)); (e) with the continuous of unloading stage, the residual-stress cracking stage tends to start, which generates the sideways-extending cracks at this stage. The reason is due to the relaxation of deformed material within the contact zone just prior to removal of the indenter superimposes intense residual tensile stresses upon the applied field (Unloading (e) in Fig. 3. (e)); (f) finally at the complete unloading stage, the lateral cracks continue to extend or may cause chipping (Unloading (f) in Fig. 3. (e)), as detailly explained by Lawn et al. (Lawn and Swain, 1975).

2.4.2. *Energy dissipation of nanoindentation*

Based on the loading curve of the nanoindentation test, the total work done can be calculated as:

$$U_t = \int Pdh \tag{5}$$

where U_t is the total work done during a nanoindentation test. Further, the total work done consists of the energy dissipated due to fracture U_f, the elastic strain energy U_e, the energy dissipated due to plastic deformation U_p and thermal energy D, which can be expressed as:

$$U_t = U_e + U_f + U_p + D \tag{6}$$

In Eq. (6), U_e is reversible but U_f, U_p, and D are irreversible. The irreversible energy dissipated during a complete loading-unloading cycle can be expressed as $U_{ir} = U_f + U_p + D$, which equals to the area between the loading-unloading curve, as illustrated as pink shaded area in Fig. 1(d).

The nonlinear loading and unloading curves are concave upwards, which can be described by power-law functions:

$$P_{l,h} = P_{max}\left(\frac{h}{h_l}\right)^n \tag{7}$$

$$P_{u,h} = P_{max}\left(\frac{h - h_f}{h_m - h_f}\right)^m \tag{8}$$

where n and m are the power indexes for the loading and unloading indentation curves.

Then, the total energy U_t and the elastic strain energy U_e can be calculated as:

$$U_t = \int_0^{h_l} P_{l,h}dh + \int_{h_l}^{h_m} P_m dh = P_m\left(h_m - \frac{n}{1+n}h_l\right) \tag{9}$$

$$U_e = \int_{h_f}^{h_m} P_{u,h}dh = \frac{P_m(h_m - h_f)}{m+1} \tag{10}$$

Subsequently, the irreversible energy ratio can be calculated as:

$$\frac{U_{ir}}{U_t} = 1 - \frac{U_e}{U_t} = 1 - \frac{(n+1)(h_m - h_f)}{(m+1)(h_m + nh_m - nh_l)} \tag{11}$$

Eq. (11) gives the irreversible energy ratio by considering the holding stage during the nanoindentation test.

3. Results and discussions

3.1. Mineralogical compositions in coal samples

From the XRD data, the weight percentages of different mineralogical compositions in three coal samples are summarized in Table 1. The contents of amorphous carbon in three coal samples account for the single largest proportions with ~93.59% (I5), ~95.72% (I6), and ~ 96.00% (P8). Additional inorganic minerals in three coal samples includes: kaolinite, ~2.32% (I5), ~1.69% (I6), and ~ 1.45% (P8); quartz, ~0.77% (I5), ~1.69%(I6), and ~ 1.67% (P8); pyrite, ~0.77% (I5), ~0.34%(I6), and ~ 0.44% (P8); calcite, ~0.11%(I6) and ~ 0.22% (P8); muscovite, ~0.22% (P8); szomolnokite, ~2.55% (I5); and gypsum, ~0.45% (I6). Based on the mineral identifications from EDS analyses, the elemental compositions of different minerals can be quantified. The obtained morphological features of minerals and the elemental compositions using FESEM-EDS were used to match with the EDS results. Thus, the structural and elemental information of the micro-areas occupied with nano-scale indents can be identified.

3.2. Characteristics of the load-displacement curves

Fig. 4 shows the load-displacement curves of the three tested coal samples. By implementing the loading-holding-unloading scheme, the nonlinear loading and unloading curves were found to be all concave upwards as figure shows. The maximum load (10000μN) was pre-set for all the load-displacement curves while the corresponding localized deformations were difference depending on the mechanical property of the corresponding given indents. Compared to Pittsburgh #8 coal sample (P8), the load-displacement curves for both samples I5 and I6 are relatively scattered indicating much more obvious features in heterogeneity and anisotropy. The nanoindentation tests in this study were load-controlled, the lateral plateaus are observed on some of the load-displacement curves such as their occurrences in samples I5 and I6, when the pop-in events occur at certain critical loads.

3.3. Acquisition of mechanical properties and morphology characteristics

Based on Eqs. (2) and (3), the Young's moduli and hardness of three coal samples I5, I6 and P8 were estimated and the results were plotted in Fig. 5 (a), (b) and (c). For sample I5, the Young's moduli at four selected locations span a wide range, from ~2.93 GPa to ~54.63 GPa, while the majority of these values were tested to be between ~2.93 GPa to ~9.78 GPa. Typically, the four extreme indents were located at the position M1 including 'M1_30' (~26.98GPa), 'M1_47' (~54.63GPa), 'M1_50' (~48.53GPa) and 'M1_51' (~32.28GPa). For sample I6, the Young's moduli range from ~2.73 GPa to ~47.10 GPa with three extreme values of ~22.34 GPa (M3_33), ~35.30 GPa (M3_17), and ~ 47.10 GPa (M3_32) and most of them gather in the range from ~2.73GPa to ~14.03GPa. By comparing with samples I5 and I6, sample P8 is more homogeneous with the Young's moduli range from ~4.93GPa to ~6.53GPa (narrowly distributed). The hardness based on Eq. (3) is approximately proportional to the Young's modulus, as shown in Fig. 5 (a), (b) and (c). The hardness of the three samples ranges from ~0.20 GPa to ~20.12 GPa for sample I5, from ~0.17 GPa to ~10.32 GPa for sample I6, and from ~0.48 GPa to ~0.71 GPa for sample P8, respectively. Both the data of the Young's moduli and hardness are very dispersed due to the heterogeneity of microstructure of different coal samples. The Gaussian distribution was used to conduct the statistical analysis. For better data visualization, the above-mentioned 7 extreme indentation points in samples I5 and I6 were excluded for the Gaussian distribution analysis mainly because these extreme indents fall on very unique structures or minerals and which will be detailly analyzed in

Table 1
Weight percentage of the mineralogical compositions in coal samples (wt%).

Compositions	Amorphous	Silicates		Sulfides	Carbonates	Phyllosilicate	Sulfate	
	Carbon	Kaolinite	Quartz	Pyrite	Calcite	Muscovite	Szomolnokite	Gypsum
I5	93.59	2.32	0.77	0.77	–	–	2.55	–
I6	95.72	1.69	1.69	0.34	0.11	–	–	0.45
P8	96.00	1.45	1.67	0.44	0.22	0.22	–	–

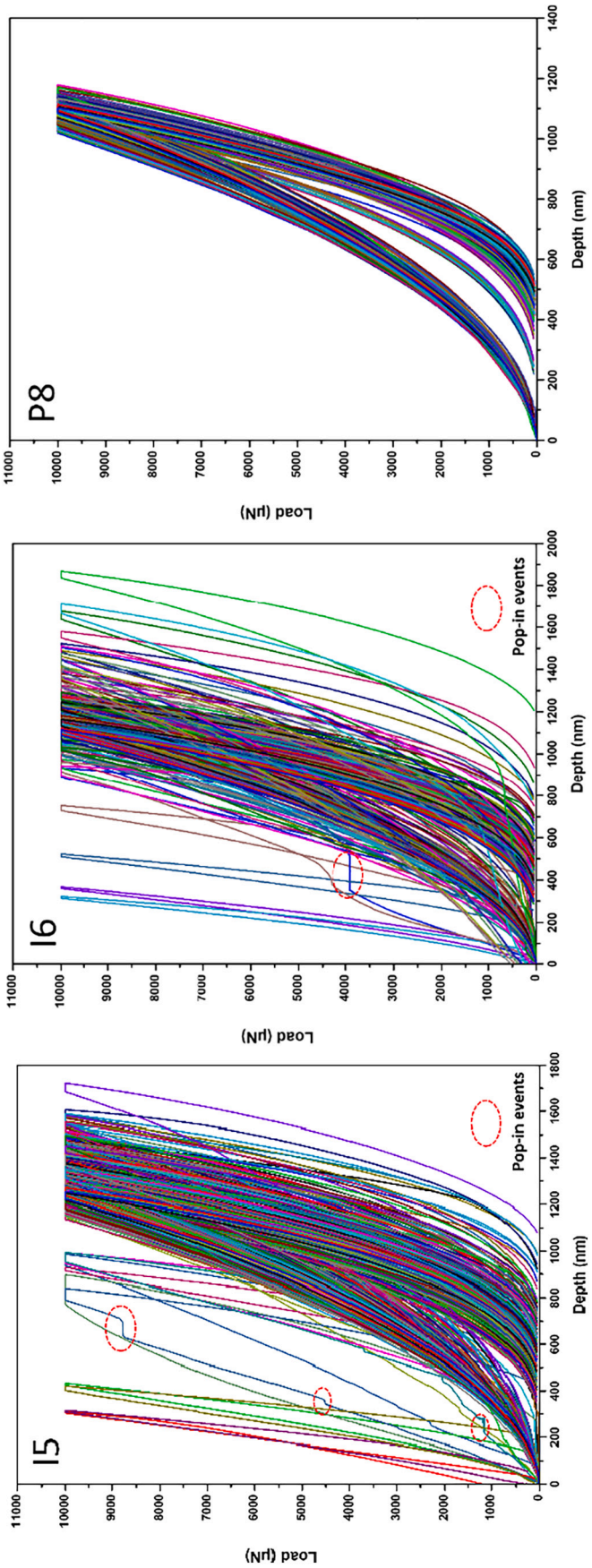

Fig. 4. Total of 256 Load-displacement curves for each one of the three samples.

following part. The mean Young's moduli and hardness of sample I5 are ~4.13 GPa and ~ 0.38 GPa respectively (Fig. 5 (a1) and (a2)), while they are ~4.79 GPa and ~ 0.49 GPa for sample I6, and ~ 5.56 GPa and ~ 0.58GPa for sample P8. By recalling the mineralogical data in Table 1, it shows that the bituminous coal (P8) and the sub-bituminous coals (I5 and I6) contain very close mineral compositions, while the Young's moduli and hardness of P8 are expected to be higher than that of sub-bituminous coals (I5 and I6) mainly because the structures and minerals in coal P8 is more uniformly distributed. The heterogeneity of sub-bituminous coals is much more apparent (coals I5 and I6) and statistically the mechanical properties of which may range significantly.

3.4. Characteristics acquisition of the morphology and composition

The morphology and composition characteristics of localized indents were identified using FESEM-EDS, as shown in Fig. 6. Except for the extreme indents, as illustrated in Fig. 5, most of indents on each sample showed very similar behaviors. We only chose to analyze two locations on each sample since mostly the morphology and composition behavior on the four locations are similar to each other and showed statistical consistency. In Fig. 6, the FESEM images (Fig. 6 (a1), (a3), (b1), (b3), (c1) and (c3)) showed the morphology characteristics of localized indents and the EDS-layered images (Fig. 6 (a2), (a4), (b2), (b4), and (c4)) exhibited the elemental distributions on the selected locations. The mapping results through the FESEM images and EDS layer helped identify the localized information of each indent. As visualized in Fig. 6 (a1), the 64 indents cover a 70μm×70μm region on which different shapes of compositions and fractures/faults were visually apparent under FESEM. The chemical elements using EDS were stacked and mapped with the mineralogical compositions in Table 1, and thus the mineral type can be identified by combining XRD and FESEM-EDS data. From Fig. 6 (a2), this region is rich of organic carbon matter but also contains the minerals such as kaolinite, pyrite. Based on Figs. 2 (a) and 6 (a1), some of the indents fell on minerals such as 'M1_09' (kaolinite-rich mineral), 'M1_30', 'M1_50', 'M1_51' (pyrite-rich mineral), et al. The information of indents on another location 'M3' on sample I5 is shown Fig. 6 (a3) and (a4). Compared to 'M1', the 64 indents on 'M3' landed on a region that is relatively homogeneous and the dominant mineral was found to be kaolinite-rich mineral. The distribution of these 64 indents is relatively uniform on organic carbon matter and it is presumed that the measured mechanical parameters should be narrowly distributed as shown in Fig. 5 (a).

In Fig. 6 (b1) and (b2), the firstly selected location 'M2' with the left two columns of indents encounter with kaolinite-rich minerals and the right six columns of indents landed on organic carbon matters. In Fig. 6 (b3) and (b4), the strip-shaped minerals constitute of quartz and kaolinite. It was observed that three indents including 'M3_17', 'M3_32', and 'M3_33' landed on a quartz-rich solid matrix. Compared to I5 and I6, sample P8 is relatively homogeneous as shown in Fig. 6 (c1) to (c2). For sample P8, the XRD analysis results shown that it contains minerals including quartz, kaolinite, pyrite, calcite, and very less muscovite. Fig. 6(c2) gives the EDS-layered nanoindentation matrix image. On this matrix area, the distributions of kaolinite can be easily identified by superimposing elemental mappings of Si, Al (method by referring Appendix A). It showed that there were some kaolinite-rich minerals at location 'M1' and they distributed over this nanoindentation matrix area. Further, the homogeneous characteristics can be observed in Fig. 6 (c4) where the organic carbon matter fully cover the whole region.

3.5. Linkage between extreme indents in mechanical properties to morphologies and compositions

From Figs. 5 and 6, the mechanical properties at various indent's sites were measured and the morphological and mineralogical characteristics of localized indents were probed. The deformation responses beneath the pointed indenter were highly related with the composition types and

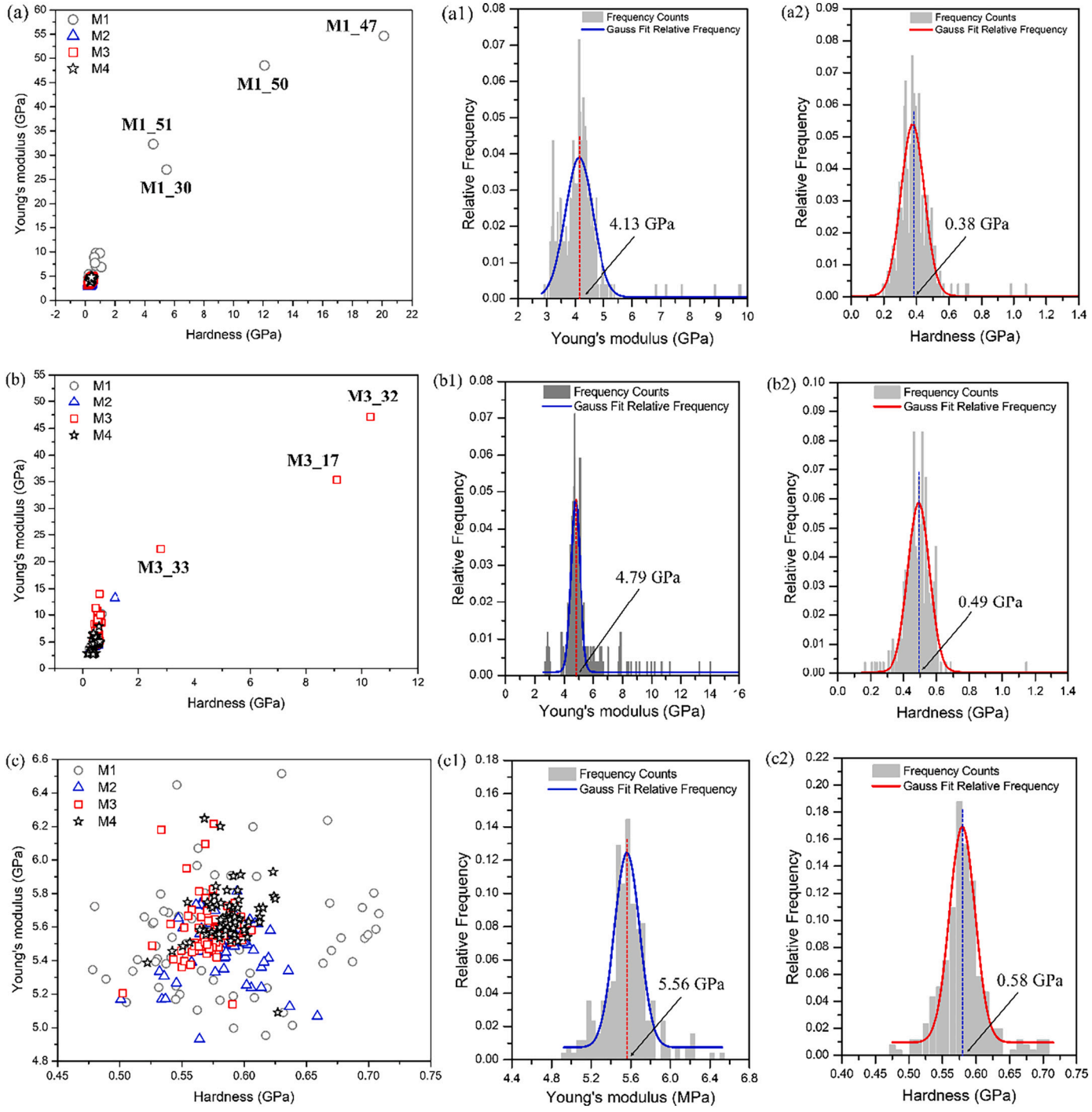

Fig. 5. Distributions of Young's moduli and Poisson's ratios at different locations. (a) I5; (b) I6; (c) P8.

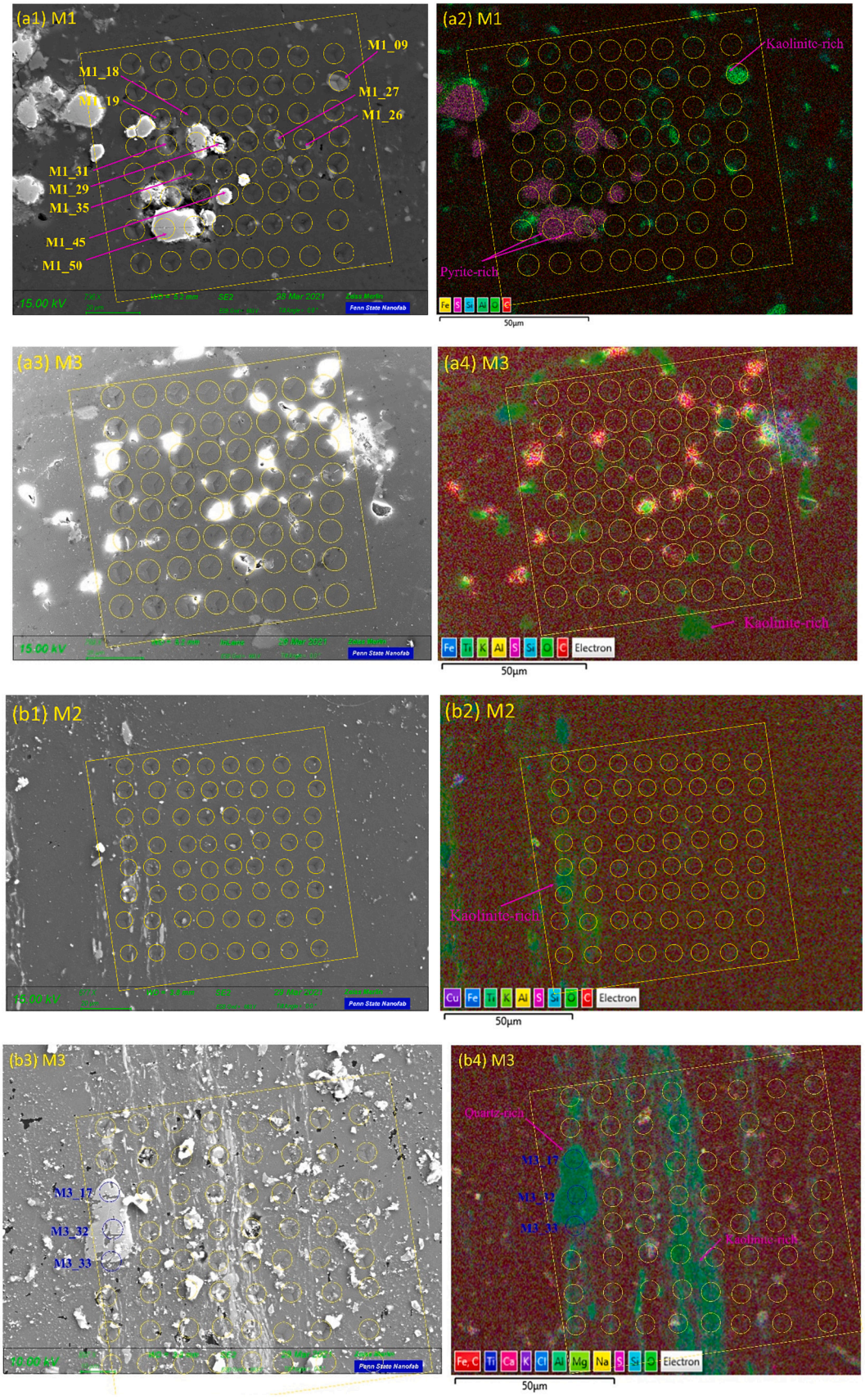

Fig. 6. Identification of morphology and composition characteristics of localized indents using FESEM-EDS: (a1) 'M1' on sample I5 and (a2) 'M3' on sample I5; (b1) 'M2' on sample I6 and (b2) 'M3' on sample I6; (c1) 'M1' on sample P8 and (c2) 'M3' on sample P8.

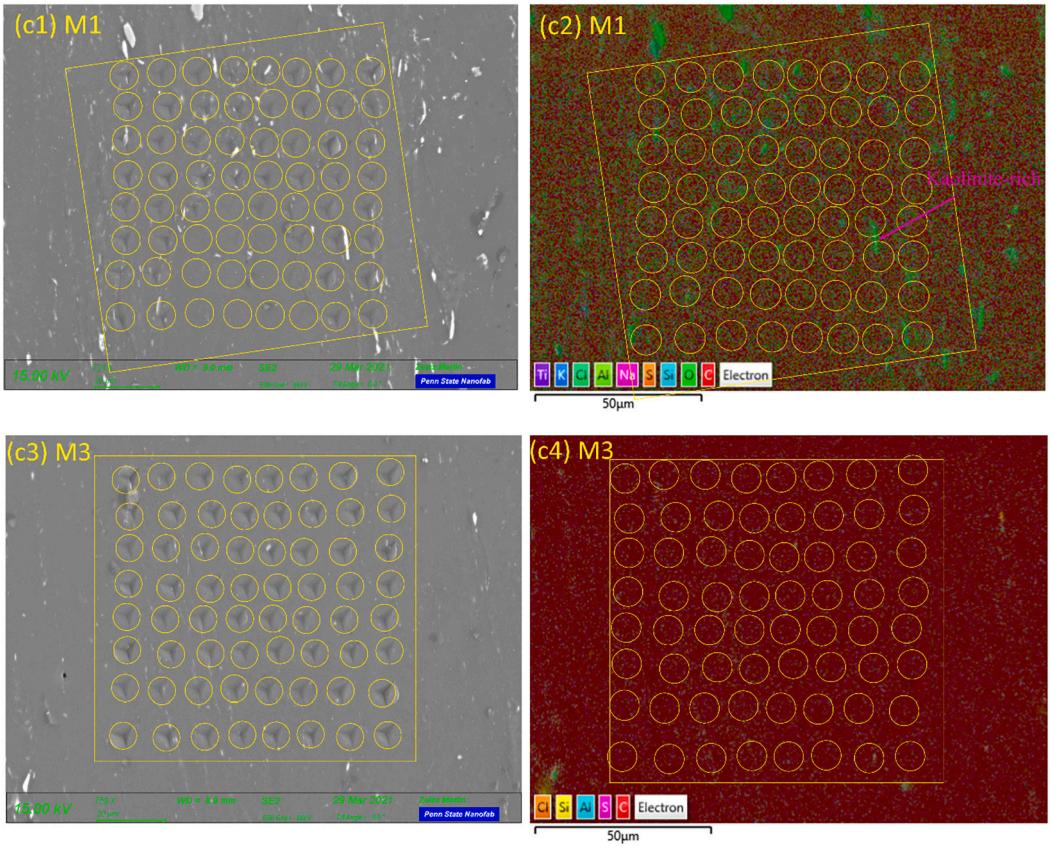

Fig. 6. (*continued*).

the localized micro-structures. Based on Fig. 5 (a), the mechanical parameters at location 'M1' showed obvious differences and the heterogeneity characteristics of morphology and composition are apparent as shown in Fig. 6 (a1) and (a2). Thus, we took the location 'M1' on sample I5 as an example for analysis. A total of ten indents ('M1_09', 'M1_18', 'M1_19', 'M1_26', 'M1_27', 'M1_29', 'M1_31', 'M1_35', 'M1_45', and 'M1_50', as shown in Fig. 6 (a1)) out of 64 indents were identified and discussed in detail here. For these ten indents, we considered the distributions of minerals, surficial micro-structures, and indent vicinity structure beneath the pointed indenter.

The characteristics of the ten indents with their morphologies and compositions were illustrated in Fig. 7 and the correspondent load-displacement curves at these locations were plotted in Fig. 8. As shown in Fig. 7, the indent 'M1_09' landed on a whole piece of kaolinite-rich mineral with the Young's modulus and hardness of 4.75 GPa and 0.43 GPa. Another indent 'M1_27' also landed on a piece of kaolinite-rich mineral with the Young's modulus and hardness of 4.57 GPa and 0.40 GPa. Both Young's modulus and hardness of 'M1_27' was found to be similar to 'M1_09' with slightly smaller values. This can be explained by the localized vicinity variation. Specifically, the indent 'M1_27' landed on the combination of half kaolinite-rich mineral and half organic carbon matter, while the indenter completed landed on the kaolinite-rich mineral at 'M1_09'. We can also observe that the kaolinite-rich minerals sporadically distribute near one indentation of indent 'M1_26' but do not gather as those visible pieces exhibited at the locations of indents of 'M1_09' and 'M1_27'. The Young's modulus and hardness of this indent 'M1_26' were 5.04 GPa and 0.39 GPa, which were a little higher than both 'M1_09' and 'M1_27' indents. In addition, it was observed that the pyrite-rich minerals spreads at indents 'M1_29', 'M1_45', and 'M1_50'.

It is visible that all these three indents landed on pyrite-rich minerals but exhibit large differences in the mechanical properties. The Young's moduli (4.73GPa ('M1_29'), 6.84GPa ('M1_45'), and 48.54GPa ('M1_50')) and hardness (0.23GPa ('M1_29'),1.08GPa ('M1_45'), and12.09GPa ('M1_50')) were measured at these three locations. This variation can be due to the localized structure for the similar mineral composition. The pyrite-rich mineral holding the indent 'M1_29' is loosely packed and its vicinity includes micro-fractures/flaws. For 'M1_45', a relatively rounded piece of pyrite-rich mineral occurred and the indenter was completely landed on it. A larger piece of pyrite-rich mineral was observed at the indent 'M1_50' and the size comparisons can be better visualized in Fig. 6 (a1). Correspondingly, the Young's modulus and hardness were found to be dramatically increased, which may be attributed the large piece of pyrite-rich mineral allow the indenter fully landed on it without being influenced by its vicinity micro-structures. Based on the results, we can safely conclude that the mechanical properties at a given indent site was highly influenced by its vicinity due to variation of mineral composition and micro-structure, as illustrated by the data from indents 'M1_18', 'M1_19', 'M1_31', and 'M1_35'.

From Fig. 7, all these indents landed on regions with pre-existed pores/fractures or flaws. It can be seen that the Young's moduli at

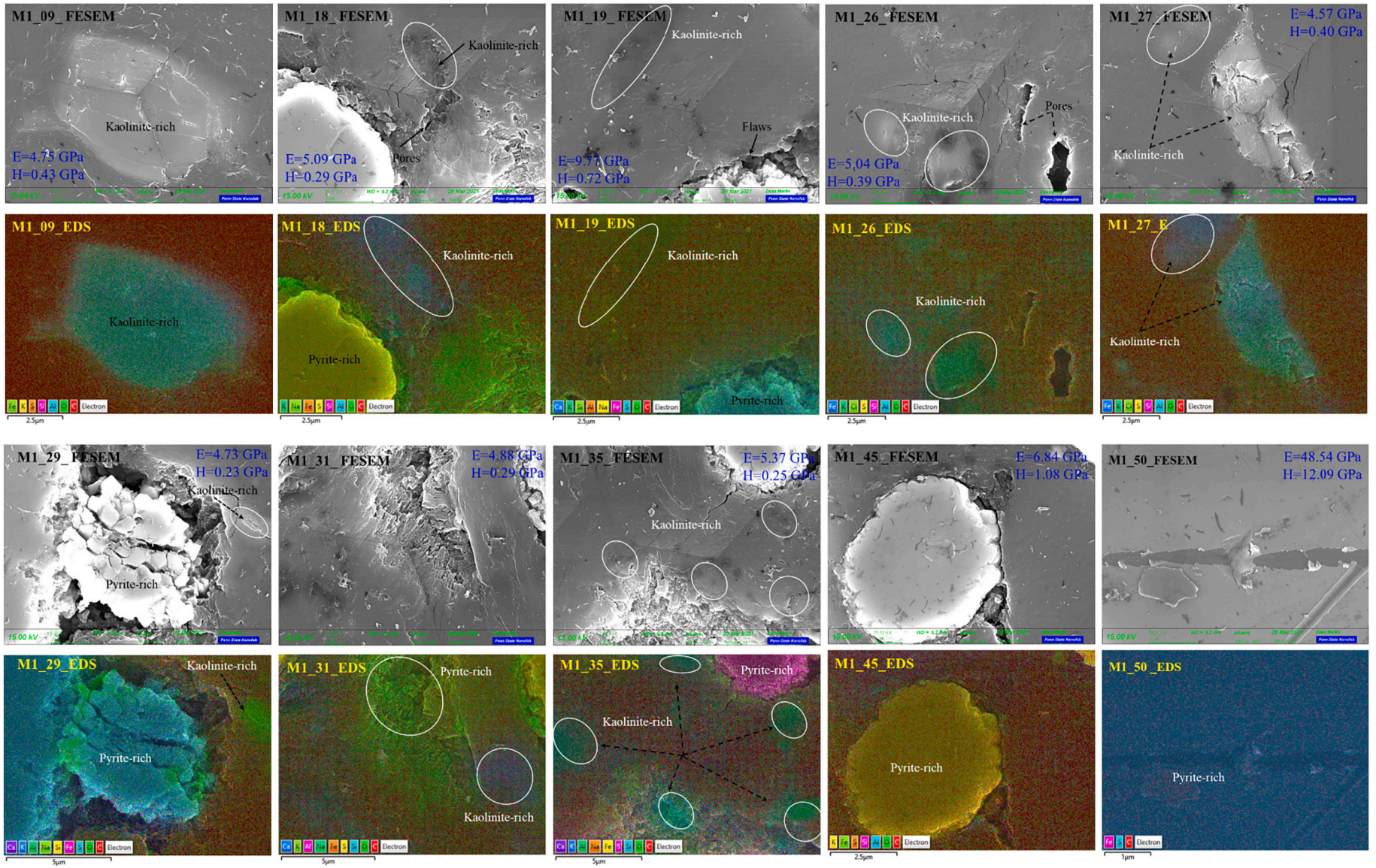

Fig. 7. Characteristics of the ten indents with their morphologies and compositions.

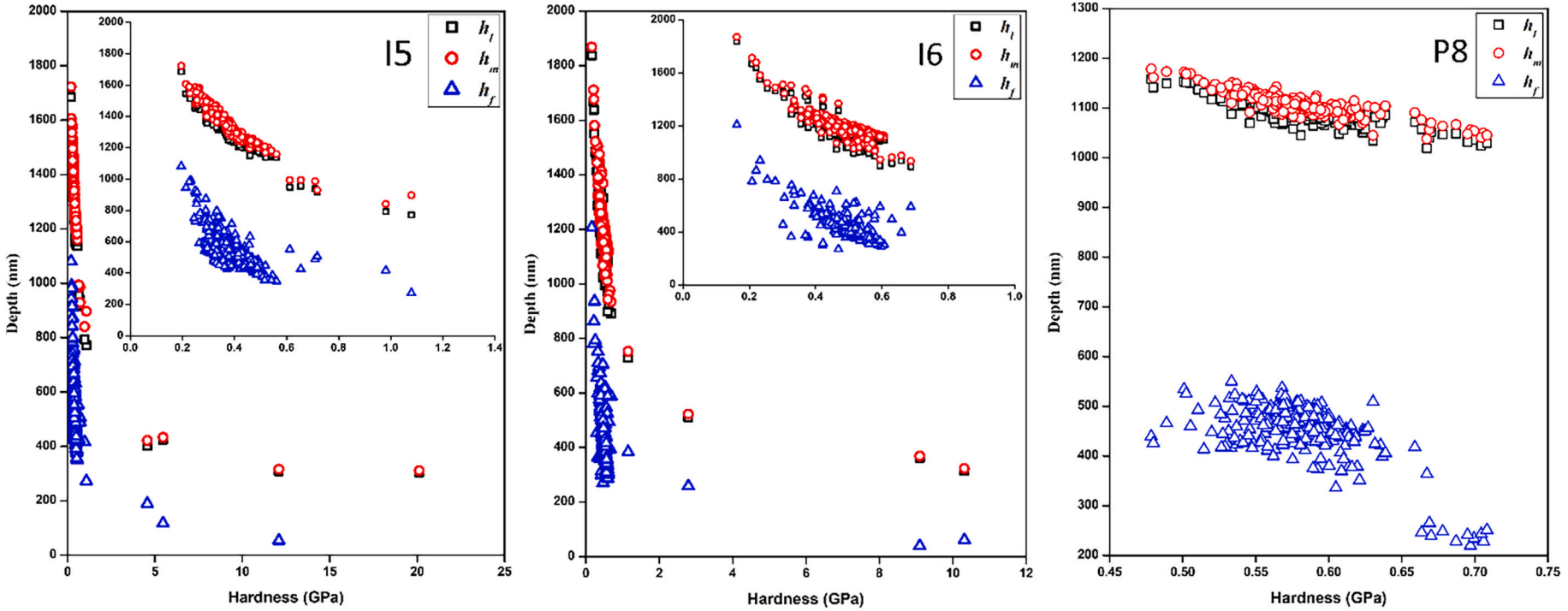

Fig. 8. Indenter depths h_l, h_m, and h_f at the loading-displacement curve.

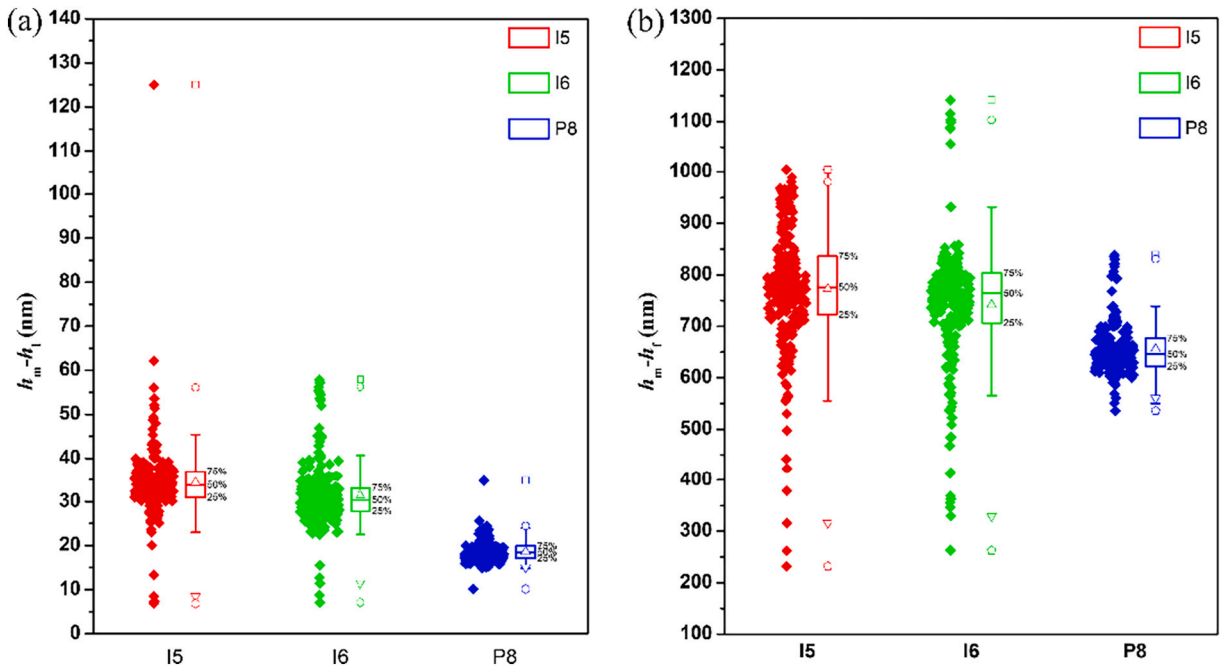

Fig. 9. Displacement differences between the indenter depths at different stages.

these four locations (5.09GPa ('M1_18'), 9.77GPa ('M1_19'), 4.88GPa ('M1_31'), and 5.37GPa ('M1_35'), respectively) and hardness (0.29GPa ('M1_18'), 0.72GPa ('M1_19'), 0.29GPa ('M1_31'), and 0.25GPa ('M1_35')) were related with the localized micro-structures. Among them, only indent 'M1_19' landed on a region free of flaws at which exhibit the highest modulus and hardness. It is also visible that the indent 'M1_31' landed on a region largely covered by pre-exists flaws exhibiting a soft-mechanical parameters, where the two sides of the indenter encounter with pre-existed flaws. Both the other two indents 'M1_18' and 'M1_31' partially meet with the pre-existed factures/flaws. The direct evidence between the mechanical responses beneath pointed indenter and the localized characteristics of indents confirmed that the nanoscale mechanical properties are highly composition- and structure-dependent.

3.6. *Deformations beneath the indenter during loading-holding-unloading*

Mechcanical deformations beneath the pointed indenter during loading-holding-unloading can be used to reflect the localized displacements/failure behavior in response to the *in situ* stressing condition. From the load-displacement curve, the depth of the indenter at the end of the loading stage (h_l), the maximum displacement (h_m), and the final depth (h_f) can be obtained and plotted with respect to hardness, as shown in Fig. 8. It is observed that all these three depths at different stages continuously decrease with the increase in hardness. The depth h_l is the deformation of coal under pointed indenter at the end of the loading stage, which incorporates both the elastic and plastic responses under the loading. At the holding stage, the maximum displacements (h_m) reached under the constant maximum load and the creep deformation is responsible for this stage (Liu and Liu, 2022). As the unloading stage proceeds, the deformation starts to recover till to the final displacement (h_f) upon the load vanishes. The three displacements of sample I5 range from ~304.24 nm to ~1684.51 nm (h_l), from ~311.11 nm to ~1721.69n m (h_m), and from ~53.65 nm to ~1080.62 nm (h_f). For sample I6, the three displacements range from ~314.52 nm to ~1837.25 nm (h_l), from ~323.27 nm to ~1868.63 nm (h_m), and from ~60.79 nm to ~1206.86 nm (h_f). For sample I6, the three displacements range from ~1018.86 nm to ~1158.16 nm (h_l), from ~1037.88 nm to ~1178.86 nm (h_m), and from ~219.84 nm to ~549.63 nm (h_f). The data shows significant fluctuations on the displacements for sample I5 and I6 caused by the significant differences in characteristics of morphology

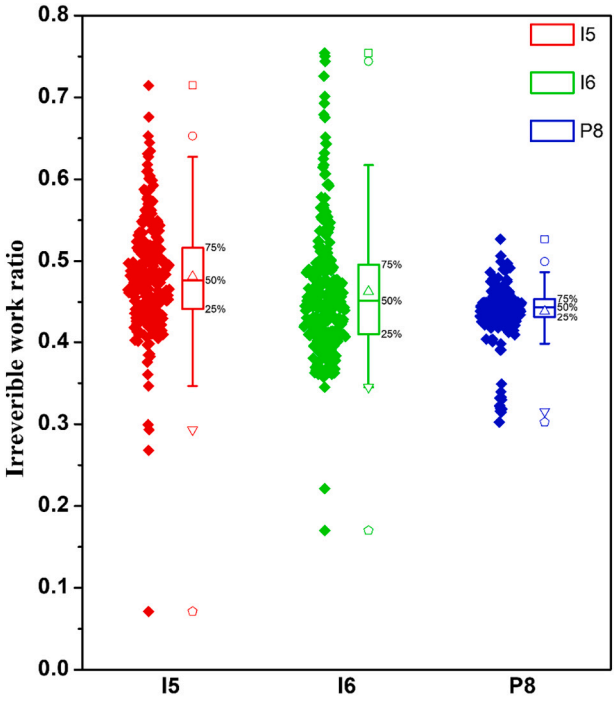

Fig. 10. Distributions of the irreversible work ratios of three samples.

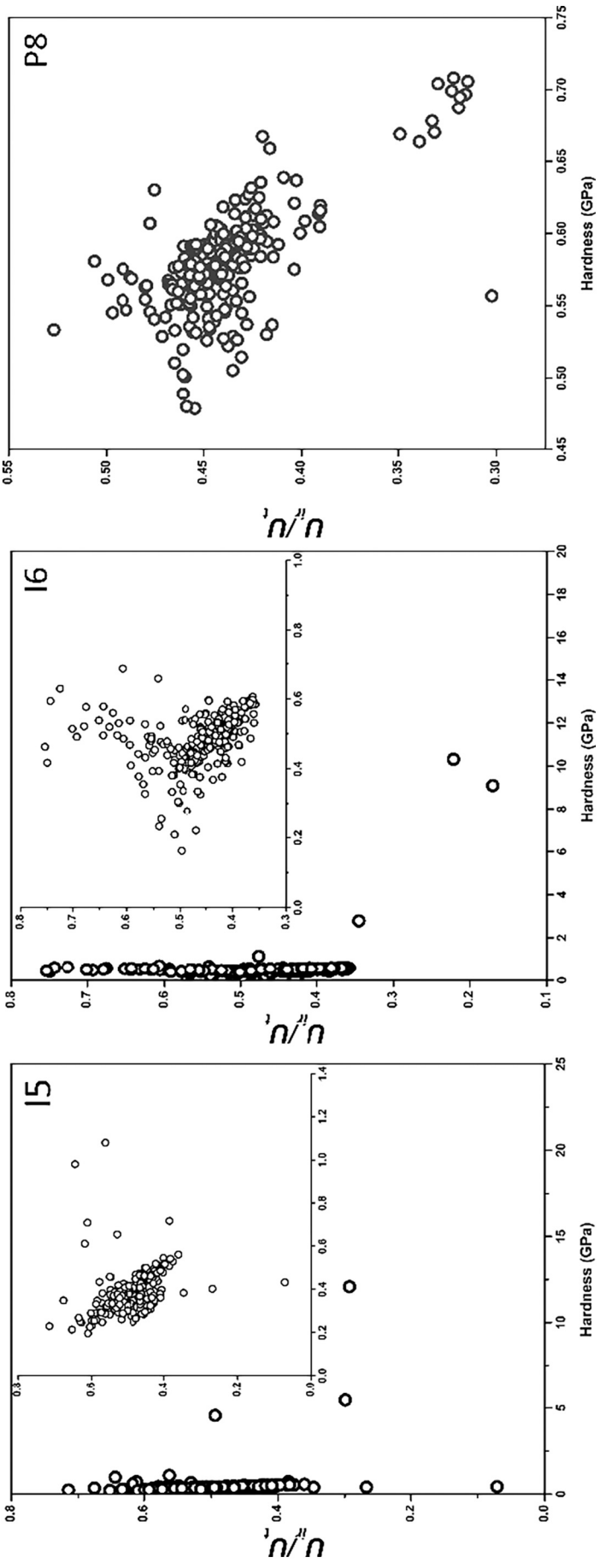

Fig. 11. Irreversible work ratios of three samples with respect to hardness.

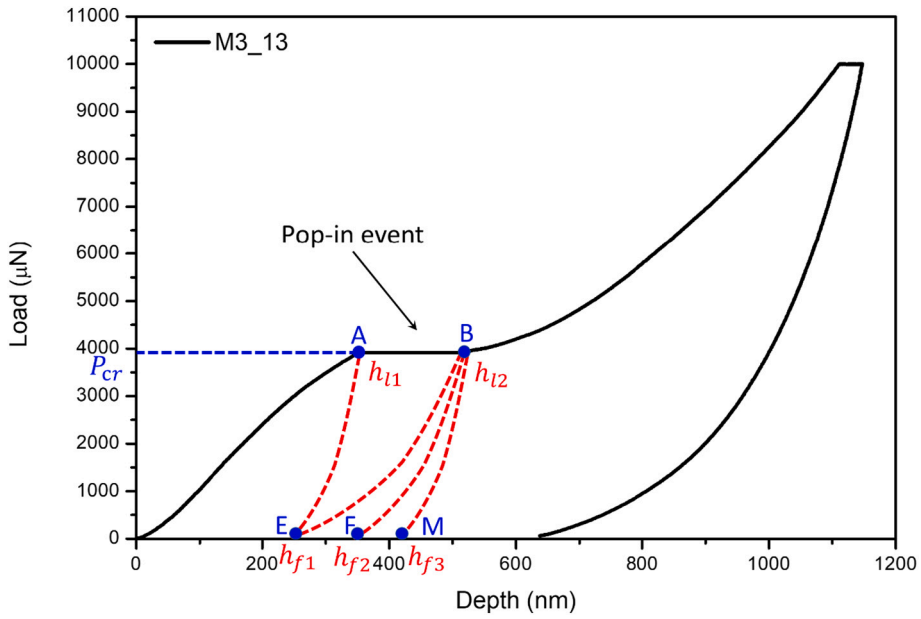

Fig. 12. Pop-in event on the load-displacement curve of indent 'M3_13' from sample I6 and the toughness limits model.

and composition among those indents as evinced in Figs. 5 to 7, while the sample P8 is relatively homogenous.

To discuss the coal-rank dependent displacement behavior of three coals, the displacement differences between the indenter depths at different stages were calculated and plotted in Fig. 9. The results showed that the creep deformations induced by the constant load at the holding stage were very close between the two sub-bituminous coals I5 and I6, and the most of displacement differences ($h_m - h_l$) from the 512 indents range from ~25 nm to ~40 nm (Fig. 9 (a)). By comparing with sub-bituminous coals, the displacement difference of the bituminous coal P8 exhibits a very narrow range from ~15 nm to ~25 nm. In other words, the bituminous coal P8 is expected to better withhold mechanical compressions under the constant load and the coal is 'hard' enough to avoid permanent deformation responses, which implicitly explains the mechanical parameters of bituminous coal P8 is larger than that of bituminous coals I5 and I6, as illustrated in Fig. 5. In Fig. 9 (b), the displacement differences ($h_m - h_f$) were calculated and plotted. The displacement differences for both sub-bituminous coals I5 and I6 were also very close from ~700 nm to ~850 nm but both exhibit significant fluctuations. For the bituminous coal P8, the recoverability ranges from ~600 nm to ~700 nm and the range narrowly distributed. By comparing with the data in Fig. 9 (a), even the bituminous coal P8 is harder than that of sub-bituminous coals I5 and I6 and can better hold the constant load. But deformation recoverability of bituminous coal (P8) is worse than sub-bituminous coals (I5 and I6). In other words, the harder bituminous coal is more brittle than sub-bituminous coal, which is expected to better in stiffer but the deformations are relatively permanent upon the deformation occur (Liu and Liu, 2022).

3.7. Analysis of the irreversible plastic work for indents

As shown in Fig. 2 (d), the amount of energy dissipated during a complete loading-unloading cycle is irreversible, which is expected to be transformed into the energy dissipated due to fracturing, the energy dissipated due to plastic deformation and the thermal energy based on Eq. (6). Based on Eq. (11), the irreversible work ratios of three samples were calculated and plotted in Fig. 10. It was observed that the average irresversible work for samples I5 and I6 is quite scattered mainly attributed to the sigificant discrepancies in struture mophologies and minerial compostions as illustraed in Figs. 5 to 7. For bituminous coal P8, the irresversible energy disspated due to the deformation responses is relatively small and its mean value is relatively smaller than that of the other two sampls. Based on the Griffith-Irwin theory (Griffith, 1921; Irwin, 1958; Manjunath and Jha, 2019), a pre-existing crack with certain length begins to grow when the stress intensity factor at the crack tip exceeds the fracture toughness K_C ($K_C = \sqrt{\frac{E_r U_f}{A_f}}$, where A_f is the surface area of fracture, U_f is the energy disspated due to fracture) of the solid matrix (Liu and Liu, 2022). We can see that the fracture toughness is proportional to the fracture energy and further the fracture energy is a partial of the total irreversible energy based on Eq. (6). Further, it is still quite chanllenge to separate the fracture energy since the plastic energy is hard to accurately quantify. Some of previous studis tried to calculte the fracture energy with the pop-in events at the load-displacement curves (Liu et al., 2016; Manjunath and Jha, 2019). If this hypothesis was taken here, based on Fig. 4, there has no/few pop-in events on the load-displacment curves of the three samples and thus the irreversibile energy work is expected to be transformed into the energy dissipated due to plastic deformation. From Fig. 10, it shows that the range interval of the plastic work ratios on sub-bituminous coals (I5 and I6) is larger than that of bituminous coal (P8) does, which means much more plastic deformation is caused in soft coal under a continous loading stage. In addtion, the irresversible work ratio with respect to the hardness is plotted in Fig. 11. It shows that the irreversible work or plastic work decreases with the increase in hardness, which confirmed that the plastic deformation is much more easy to be caused.

3.8. Discussions on the pop-in events in the load-displacement curves

As is shown in Fig. 12, a pop-in event occurs on the on the load-

displacement curve of indent 'M3_13' from sample I6, which is a sudden displacement burst during the loading of an indenter on a sample. The nanoindentation experiment is load-controlled in this study, a horizontal plateau is observed on the load-displacement curve when a pop-in occurs at the critical load (P_{cr}). The pop-in event can be attributed with many occasions for porous coals. As examples, when the indenter encounter with a void pore/facture volume element, the sudden deformation energy release from the indenter tip can be triggered. A creep deformation continues to accumulate until the tip had gone through the pore and reached the resistant matrix or inclusion.

Based on the results in Fig. 7, the adjacent surroundings of an indent location can also trigger a pop-in event. If the deformation beneath the pointed indenter leads to the localized region separating with its adjacent surroundings, the localized region holding the indent becomes as isolated 'island' (see the indent 'M1_45' in Fig. 7) and the pop-in event is easy to occur there. In addition, the crack(s) formation with the signal of a pop-in event is widely accepted. Upon the stress intensity exceeds the fracture toughness of the volume element, the grows of crack at a pre-existing crack or begins from a volume element belongs to the original solid matrix. If the occurrence of a pop-in can be attributed to crack(s) formation (Bull, 2011; Hervas et al., 2016; Malzbender and De With, 2001), the fracture toughness is expected to be calculated using the energy-based method. Even there is a lack of consensus on the use of the energy method and even its applicability for toughness determination (Zhang and Zhang, 2012a; X. Zhang and Zhang, 2012b), the lower and upper bounds of energy for a pop-in event is widely used to calculate the fracture energy based on the imaginary curves of unloading before and after the fracture event (Chen, 2012; Liu et al., 2016; Manjunath and Jha, 2019). Based on the proposed approach by Chen et al. (Chen, 2012), it is presumed that the stiffness does not decrease after the pop-in, *i.e.* BM is parallel to AE, which gives the upper bound of the fracture dissipated energy as shown in Fig. 12. The areas ABE and ABME are regarded as the lower and upper bound of the fracture dissipated energy, respectively. Based on the fracture dissipated energy, the fracture toughness cannot be accurately calculated but it is easy to see that this parameter can only fall in a range instead of a specific value. However, there still has no direct evidence explain the complex reasons behind the pop-in events for porous coals. Future work using digital volume correlation analysis of time-resolved X-ray microtomography scans acquired during *in situ* nanoindentation test of coal micro-pillars or microscale specimen is recommended to provide time series of 3-D incremental strain fields that elucidated evolving deformation processes by quantifying microscopic strain localization.

4. Summary and conclusions

(1) The direct evidence between the mechanical responses beneath the indenter and the localized characteristics of indents confirmed that the nanoscale mechanical properties are compositional and microstructural dependent.

(2) The mean Young's moduli and hardness of two sub-bituminous and bituminous coals are ~4.13 GPa, ~4.79 GPa, and ~ 5.56 GPa respectively and the mean hardness of which are ~0.38 GPa, ~0.49 GPa and ~ 0.58 GPa respectively. The heterogeneity of sub-bituminous coals is much more obvious and statistically the mechanical properties of which may range much more significant than bituminous coal does. Therefore, it is riskier that the sub-bituminous coal formation tends to occur localized failures and the associated permeability damage than bituminous coal formation during the hydraulic fracturing stimulation.

(3) The 'harder' bituminous coal is more brittle than sub-bituminous coal, which is expected to better withhold the mechanical responses but the deformations are relatively permanent upon the deformation occur. The energy dissipation data shown that the irreversible work or plastic work decreases with the increase in hardness, which confirmed that the plastic deformation is much more easily to be caused.

(4) The mechanism-based phenomenon pop-in event on the load-displacement curve was also analyzed by linking with the characteristics of the morphology and composition beneath a pointed indenter or cracks formation due to the localized indent. Based on the fracture dissipated energy, the fracture toughness cannot be accurately calculated but it is easy to see that this parameter can only fall in a range instead of a specific value. However, there still has no direct evidence explain the complex reasons behind the pop-in events for porous coals.

Author statement

All persons who meet authorship criteria are listed as authors, and all authors certify that they have participated sufficiently in the work to take public responsibility for the content, including participation in the concept, design, analysis, writing, or revision of the manuscript. Furthermore, each author certifies that this material or similar material has not been and will not be submitted to or published in any other publication before its appearance in the *International Journal of Coal Geology*.

Declaration of Competing Interest

The authors declare that they have no known competing financial interests or personal relationships that could have appeared to influence the work reported in this paper.

Acknowledgement

This work was financially supported by National Institute for Occupational Safety and Health (NIOSH) under contract No. NIOSH-75D30119C05128.

Appendix A

FESEM-EDS and XRD are combined to match the elemental distribution layers and the potential mineral crystalline solids. As an example, the XRD fitting for coal I6 was conducted to identify the mineral crystalline compositions in coal, and thus the elemental compositions of different minerals based on their chemical expressions, as shown in Fig. A1. The EDS layered FESEM image containing a matrix of indents was shown in Fig. A2 (a), and the elemental distribution spectrum was plotted in Fig. A2 (b). Further, the overlapped elemental layers can be separated in Fig. A3. From Fig. A3, it can be very obvious to identify the occurrence of pyrite (location 'L1' in Fig. A2) by combining elemental layers of sulfur (S) and iron (Fe). Because location 'L1' contains chemical elements 'C', 'O', 'Fe', 'S' and the possible crystalline solid there should be pyrite-rich mineral based on Fig. A1.

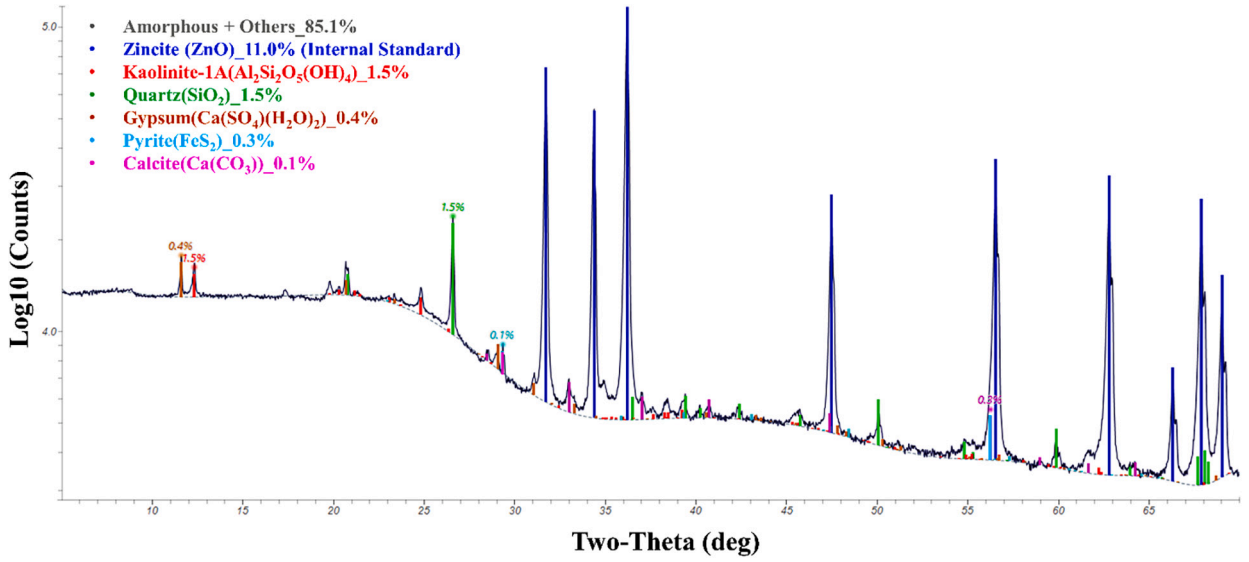

Fig. A1. Mineral composition identification using XRD fitting (I6).

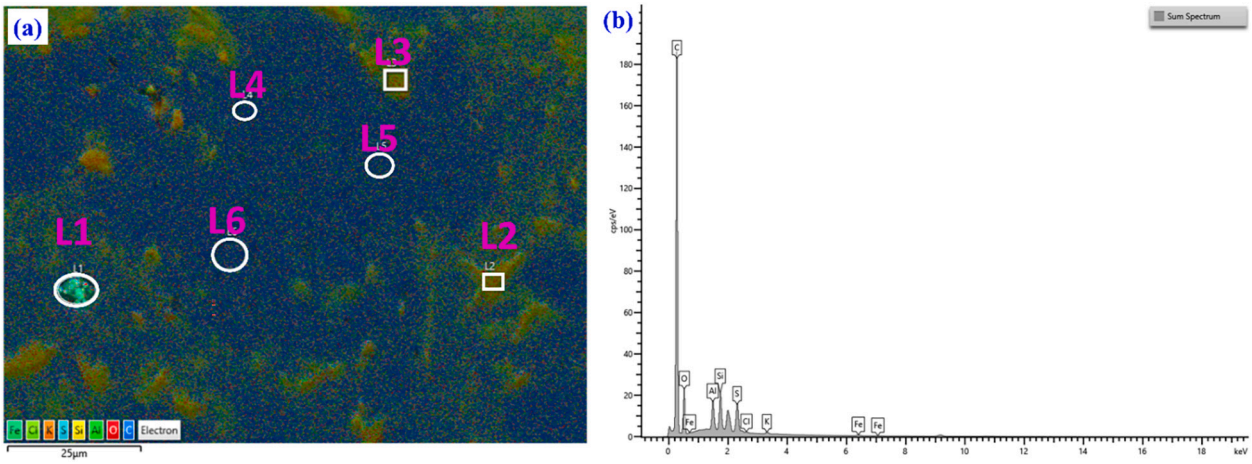

Fig. A2. EDS layered FESEM images (a) and elemental distribution spectrum (b).

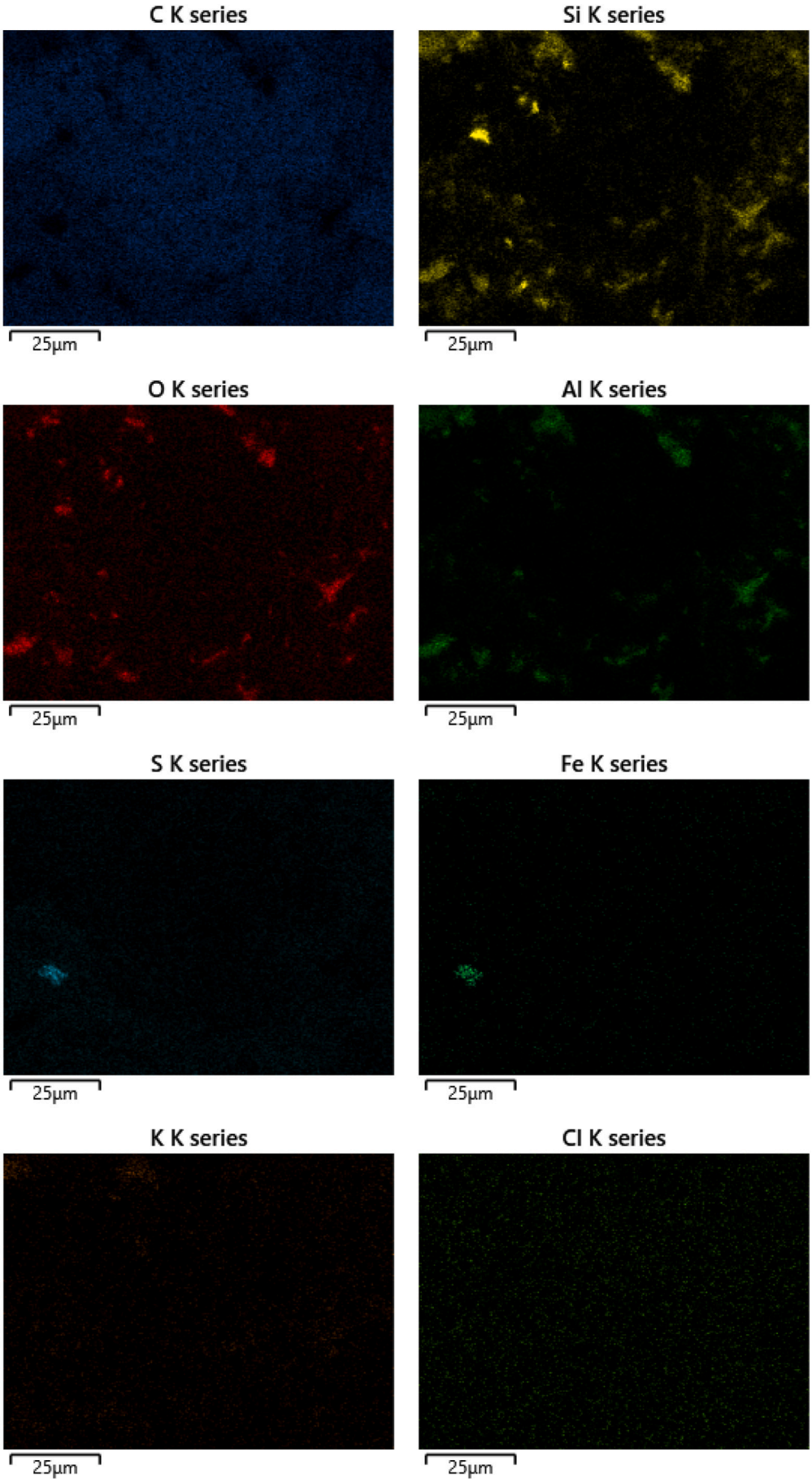
C K series
25μm
Si K series
25μm
O K series
25μm
Al K series
25μm
S K series
25μm
Fe K series
25μm
K K series
25μm
Cl K series
25μm

Fig. A3. Specified elemental distribution including carbon (C), oxygen (O), silicon (Si), aluminum (Al), sulfur (S), potassium (K), iron (Fe), and chlorine (Cl).

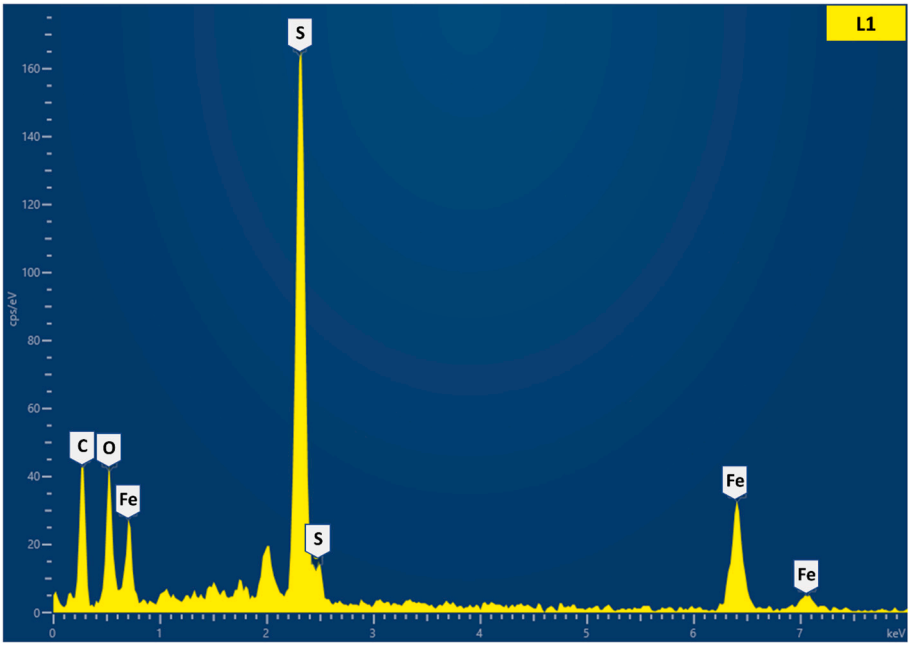

Fig. A4. Specified elemental distribution spectrum for selected area from Fig. A2.

References

Bandyopadhyay, K., Mallik, J., Ghosh, T., 2020. Dependence of fluid flow on cleat aperture distribution and aperture–length scaling: a case study from Gondwana coal seams of Raniganj Formation, Eastern India. Int. J. Coal Sci. Technol. 7, 133–146. https://doi.org/10.1007/s40789-019-00291-2.

Bull, S.J., 2011. Analysis methods and size effects in the indentation fracture toughness assessment of very thin oxide coatings on glass. Comptes Rendus - Mec. 339, 518–531. https://doi.org/10.1016/j.crme.2011.05.009.

Chen, J., 2012. On the determination of coating toughness during nanoindentation. Surf. Coat. Technol. 206, 3064–3068. https://doi.org/10.1016/j.surfcoat.2011.12.006.

Dou, L., Yang, K., Chi, X., 2021. Fracture behavior and acoustic emission characteristics of sandstone samples with inclined precracks. Int. J. Coal Sci. Technol. 8, 77–87. https://doi.org/10.1007/s40789-020-00344-x.

Epshtein, S.A., Borodich, F.M., Bull, S.J., 2015. Evaluation of elastic modulus and hardness of highly inhomogeneous materials by nanoindentation. Appl. Phys. A Mater. Sci. Process. 119, 325–335. https://doi.org/10.1007/s00339-014-8971-5.

Fischer-Cripps, A.C., 2011. Mechanical Engineering Series: Nanoindentation. Springer.

Furnémont, Q., Kempf, M., Jacques, P.J., Göken, M., Delannay, F., 2002. On the measurement of the nanohardness of the constitutive phases of TRIP-assisted multiphase steels. Mater. Sci. Eng. A 328, 26–32. https://doi.org/10.1016/S0921-5093(01)01689-6.

Griffith, A.A., 1921. The phenomena of rupture and flow in solids. Philos. Trans. R. Soc. Lond. Ser. A 221, 163–198.

Hervas, I., Montagne, A., Van Gorp, A., Bentoumi, M., Thuault, A., Iost, A., 2016. Fracture toughness of glasses and hydroxyapatite: a comparative study of 7 methods by using Vickers indenter. Ceram. Int. 42, 12740–12750. https://doi.org/10.1016/j.ceramint.2016.05.030.

Huang, H., Yan, J., 2015. New insights into phase transformations in single crystal silicon by controlled cyclic nanoindentation. Scr. Mater. 102, 35–38. https://doi.org/10.1016/j.scriptamat.2015.02.008.

Irwin, G.R., 1958. Fracture. In: Flugge, S. (Ed.), Handbuch der Physik, vol. 6. Springer-Verlag, Berlin, pp. 551–590.

Javaid, F., Xu, Y., Durst, K., 2020. Local analysis on dislocation structure and hardening during grain boundary pop-ins in tungsten. J. Mater. Sci. 55, 9597–9607. https://doi.org/10.1007/s10853-020-04655-x.

Jin, T., Niu, X., Xiao, G., Wang, Z., Zhou, Z., Yuan, G., Shu, X., 2015. Effects of experimental variables on PMMA nano-indentation measurements. Polym. Test. 41, 1–6. https://doi.org/10.1016/j.polymertesting.2014.09.015.

Kasyap, S.S., 2021. Application of Nanoindentation in the Characterization of a Porous Material with a Clastic Texture.

Kim, B.H., Walton, G., Larson, M.K., Berry, S., 2021. Investigation of the anisotropic confinement-dependent brittleness of a Utah coal. Int. J. Coal Sci. Technol. 8, 274–290. https://doi.org/10.1007/s40789-020-00364-7.

Kossovich, E.L., Borodich, F.M., Epshtein, S.A., Galanov, B.A., Minin, M.G., Prosina, V.A., 2019. Mechanical, structural and scaling properties of coals: depth-sensing indentation studies. Appl. Phys. A Mater. Sci. Process. 125, 1–15. https://doi.org/10.1007/s00339-018-2282-1.

Lawn, B.R., Swain, M.V., 1975. Microfracture beneath point indentations in brittle solids. J. Mater. Sci. 10, 113–122. https://doi.org/10.1007/BF00541038.

Li, Y., Chen, J., Elsworth, D., Pan, Z., Ma, X., 2022a. Nanoscale mechanical property variations concerning mineral composition and contact of marine shale. Geosci. Front. 13, 101405 https://doi.org/10.1016/j.gsf.2022.101405.

Li, Y., Chen, J.Q., Yang, J.H., Liu, J.S., Tong, W.S., 2022b. Determination of shale macroscale modulus based on microscale measurement: a case study concerning multiscale mechanical characteristics. Pet. Sci. 19, 1262–1275. https://doi.org/10.1016/j.petsci.2021.10.004.

Li, Y., Pan, S., Ning, S., Shao, L., Jing, Z., Wang, Z., 2022c. Coal measure metallogeny: Metallogenic system and implication for resource and environment. Sci. China Earth Sci. 65, 1211–1228. https://doi.org/10.1007/s11430-021-9920-4.

Liu, S., Harpalani, S., 2014. Evaluation of in situ stress changes with gas depletion of coalbed methane reservoirs. J. Geophys. Res. Solid Earth 6263–6276 doi:10.1002/.

Liu, A., Liu, S., 2022. Mechanical property alterations across coal matrix due to water-CO_2 treatments: a micro-to-nano scale experimental study. Energy 248, 123575. https://doi.org/10.1016/j.energy.2022.123575.

Liu, K., Ostadhassan, M., Bubach, B., 2016. Applications of nano-indentation methods to estimate nanoscale mechanical properties of shale reservoir rocks. J. Nat. Gas Sci. Eng. 35, 1310–1319. https://doi.org/10.1016/j.jngse.2016.09.068.

Liu, A., Liu, S., Wang, G., Sang, G., 2020. Modeling of coal matrix apparent strains for sorbing gases using a transversely isotropic approach. Rock Mech. Rock. Eng. https://doi.org/10.1007/s00603-020-02159-3.

Liu, A., Liu, S., Liu, P., Harpalani, S., 2021. The role of sorption-induced coal matrix shrinkage on permeability and stress evolutions under replicated in situ condition for CBM reservoirs. Fuel 294, 120530. https://doi.org/10.1016/j.fuel.2021.120530.

Lu, M., Connell, L., 2016. Coal failure during primary and enhanced coalbed methane production - theory and approximate analyses. Int. J. Coal Geol. 154–155, 275–285. https://doi.org/10.1016/j.coal.2016.01.008.

Lu, M., Connell, L., 2020. Coal seam failure during primary/enhanced gas production: how failure develops in fields. Int. J. Coal Geol. 221, 103432 https://doi.org/10.1016/j.coal.2020.103432.

Ma, Z., Ranjith, P.G., Zhang, C., 2020. Application of nanoindentation technology in rocks: a review. Geomech. Geophys. Geo-Energy Geo-Resour. 6 (4), 1–27. https://doi.org/10.1007/s40948-020-00178-6.

Malzbender, J., De With, G., 2001. The use of the indentation loading curve to detect fracture of coatings. Surf. Coat. Technol. 137, 72–76. https://doi.org/10.1016/S0257-8972(00)01091-4.

Manjunath, G.L., Jha, B., 2019. Nanoscale fracture mechanics of Gondwana coal. Int. J. Coal Geol. 204, 102–112. https://doi.org/10.1016/j.coal.2019.02.007.

Masłowski, M., Labus, M., 2021. Preliminary Studies on the Proppant Embedment in Baltic Basin Shale Rock. Rock Mech. Rock. Eng. 54, 2233–2248. https://doi.org/10.1007/s00603-021-02407-0.

Mercier, D., Mandrillon, V., Parry, G., Verdier, M., Estevez, R., Bréchet, Y., Maindron, T., 2017. Investigation of the fracture of very thin amorphous alumina film during

spherical nanoindentation. Thin Solid Films 638, 34–47. https://doi.org/10.1016/j.tsf.2017.07.040.
Oliver, W.C., Pharr, G.M., 1992. An improvved techniques for determining Hardness and elastic modulus using load and displacement sensing indentation experiments, 7, pp. 1564–1583.
Oliver, D.J., Bradby, J.E., Williams, J.S., 2007. Giant pop-ins and amorphization in germanium during indentation. J. Appl. Phys. 101, 043524.
Pethica, J.B., Tabor, D., 1979. Contact of characterised metal surfaces at very low loads: Deformation and adhesion. Surf. Sci. 89, 182–190.
Pöhl, F., 2019. Pop-in behavior and elastic-to-plastic transition of polycrystalline pure iron during sharp nanoindentation. Sci. Rep. 9, 1–12. https://doi.org/10.1038/s41598-019-51644-5.
Prasad, M., Kopycinska, M., Rabe, U., Arnold, W., 2002. Measurement of Young's modulus of clay minerals using atomic force acoustic microscopy. Geophys. Res. Lett. 29, 2–5. https://doi.org/10.1029/2001GL014054.
Sharma, P., Prakash, R., Abedi, S., 2019. Effect of temperature on nano- and microscale creep properties of organic-rich shales. J. Pet. Sci. Eng. 175, 375–388. https://doi.org/10.1016/j.petrol.2018.12.039.
Shi, X., Jiang, S., Wang, Z., Bai, B., Xiao, D., Tang, M., 2020a. Application of nanoindentation technology for characterizing the mechanical properties of shale before and after supercritical CO_2 fluid treatment. J. CO_2 Util. 37, 158–172. https://doi.org/10.1016/j.jcou.2019.11.022.
Shi, X., Jiang, S., Yang, L., Tang, M., Xiao, D., 2020b. Modeling the viscoelasticity of shale by nanoindentation creep tests. Int. J. Rock Mech. Min. Sci. 127, 104210 https://doi.org/10.1016/j.ijrmms.2020.104210.
Sneddon, I.N., 1965. The relation between load and penetration in the axisymmetric boussinesq problem for a punch of arbitrary profile. Int. J. Eng. Sci. 3, 47–57. https://doi.org/10.1016/0020-7225(65)90019-4.
Szlufarska, I., Kalia, R.K., Nakano, A., Vashishta, P., 2004. Nanoindentation-induced amorphization in silicon carbide. Appl. Phys. Lett. 85, 378.
Timoshenko, S., Goodier, J.N., 1951. Theory of Elasticity, 2nd ed. McGraw-Hill, N.Y.
Veytskin, Y.B., Tammina, V.K., Bobko, C.P., Hartley, P.G., Clennell, M.B., Dewhurst, D. N., Dagastine, R.R., 2017. Micromechanical characterization of shales through nanoindentation and energy dispersive x-ray spectrometry. Geomech. Energy Environ. 9, 21–35. https://doi.org/10.1016/j.gete.2016.10.004.
Wang, M.G., Ngan, A.H.W., 2004. Indentation strain burst phenomenon induced by grain boundaries in niobium. J. Mater. Res. 19, 2478–2486. https://doi.org/10.1557/JMR.2004.0316.
Wang, L., Zhang, Y., Wu, W., 2019. Influence factors of pop-in in the nanoindentation micromechanical property measurement of gas-bearing shale. Mater. Test. 61, 973–980.
Wang, D., Lu, X., Lin, M., Wan, D., Li, Z., He, J., Johnsen, R., 2022. Understanding the hydrogen effect on pop-in behavior of an equiatomic high-entropy alloy during in-situ nanoindentation. J. Mater. Sci. Technol. 98, 118–122. https://doi.org/10.1016/j.jmst.2021.04.060.
Zeng, Q., Feng, Y., Xu, S., 2017. A discussion of "Application of nano-indentation methods to estimate nanoscale mechanical properties of shale reservoir rocks" by K Liu, M Osatadhassan and B Bubach. J. Nat. Gas Sci. Eng. 42, 187–189. https://doi.org/10.1016/j.jngse.2017.02.027.
Zhang, S., Zhang, X., 2012a. Toughness evaluation of hard coatings and thin films. Thin Solid Films 520, 2375–2389. https://doi.org/10.1016/j.tsf.2011.09.036.
Zhang, X., Zhang, S., 2012b. Rethinking the role that the "step" in the load-displacement curves can play in measurement of fracture toughness for hard coatings. Thin Solid Films 520, 3423–3428. https://doi.org/10.1016/j.tsf.2011.12.056.
Zhang, Y., Lebedev, M., Al-Yaseri, A., Yu, H., Xu, X., Iglauer, S., 2018. Characterization of nanoscale rockmechanical properties and microstructures of a Chinese sub-bituminous coal. J. Nat. Gas Sci. Eng. 52, 106–116. https://doi.org/10.1016/j.jngse.2018.01.037.
Zuo, J., Wang, J., Jiang, Y., 2019. Macro/meso failure behavior of surrounding rock in deep roadway and its control technology. Int. J. Coal Sci. Technol. 6, 301–319. https://doi.org/10.1007/s40789-019-0259-0.